Paper wcd-2020-26

"Vertical cloud structure of warm conveyor belts – a comparison and evaluation of ERA5 reanalyses, CloudSat and CALIPSO data"

by Hanin Binder, Maxi Boettcher, Hanna Joos, Michael Sprenger and Heini Wernli

Response to the Reviewer's comments:

We thank both reviewers for their constructive reviews that helped to improve our manuscript. We did our best to follow the suggestions. Essentially, we have made the following important changes:

- To ease the understanding, we have included a schematic illustration of the method to attribute several satellite profiles to a matching ERA5-based WCB trajectory in the climatological analysis (comment of reviewer 1).
- We have included a brief discussion of the radar dim band at the melting layer, which is characteristic for millimetre-wavelength radars like CloudSat (comment of reviewer 1).
- Thanks to a comment of reviewer 2, we found a data gap around 170°W and incorporated the missing data in the climatological analysis. The updated figures are almost identical to those in the previous version, such that the inclusion of the missing data does not affect the findings of this study.
- We have included a discussion of the uncertainties in the satellite-retrieved IWC values (comment of reviewer 2).

Below are the detailed replies to the individual comments.

Reviewer 1 (Josué Gehring)

General comments

The authors investigate the cloud and precipitation associated with WCBs during nine Northern Hemisphere winters with ERA5 reanalyses, CloudSat and CALIPSO data. They use ERA5 to not only depict the meteorological conditions associated with these WCB-produced cloud systems, but also to compare its performance with the measurements. They provide novel findings on the climatology of clouds and precipitation associated with WCBs and their corresponding thermodynamical and dynamical fields. In particular, the small- and mesoscale structures depicted with the satellite measurements are unprecedented. I strongly support the conclusions of this study and its publication in Weather and Climate Dynamics, subject to minor revisions.

Specific comments

L.29. "[...], which can intensify the associated cyclone (Binder et al., 2016)"
Maybe you could add Davis and Emanuel, 1991; Rossa et al., 2000.

Reply: Thank you, we now mention these studies as well.

L. 51, 54: Blanchard et al. 2020 could be added either on L. 51 or 54 along with Oertel et al. 2019 or 2020 respectively, since it is also an example of embedded convection in a WCB during NAWDEX, respectively an example of mesoscale PV dipoles.

Reply: This is true, we now mention Blanchard et al. 2020 along with Oertel et al. 2019.

L.106-107: The sensitivity of the CPR ranges from −30 to 50 dBZ. This is quite a large interval, could you give an indication of the sensitivity as a function of range (e.g. -30 dBZ at X m a.s.l., 50 dBZ at Y m a.s.l.)? I guess the sensitivity of 50 dBZ is in the case of attenuation?

Reply: We apologize, this sentence was confusing, we wanted to say that the minimum detectable reflectivity is -30 dBZ and the maximum 50 dBZ. However, we will now just mention the minimum, as the maximum is not important for our study. We changed the sentence to: "The minimum detectable signal of the CPR is -30 dBZ."

L. 108: [...], which can amount to more than 10 dBZ km-1 [...]
Could you give a value or just a qualitative statement of the attenuation if no liquid water is present? Even at 94 GHz, the attenuation by gases and ice is much smaller than the one of liquid water. This would help a reader not familiar to radar attenuation to understand that it is less significant above the melting layer (respectively above the highest supercooled liquid water layer).

Reply: Unfortunately, we could not find more quantitative information about attenuation in situations without liquid water. In order to emphasize the point that attenuation by liquid water is more relevant, we changed the sentence to "Absorption mainly by liquid water results in a two-way attenuation of the radar signal, which can amount to more than 10 dBZ km^{-1} below the melting layer and even lead to a full attenuation of the radar signal in strongly precipitating systems (Mace et al., 2007; Marchand et al., 2008)."

L. 159-170: I like the modifications to identify the WCB with respect to Madonna et al. (2014) method, I think it makes totally sense. However a 45% total increase of the number of trajectories is quite substantial. Could you explain a bit the motivation behind these modifications? Is it motivated specifically by the aim of this study or should it apply to all future WCB detections? Do you expect your results to be sensitive to this increase in the number of trajectories? For instance, it could modify the distribution of the type of WCB included (e.g. more rapidly ascending ones with respect to Madonna et al. (2014) method).

Reply: These modifications with respect to the original method are not specifically motivated by the aim of this study, but they will be used in all our future studies based on ERA5. When calculating the new WCB climatology in ERA5 we took the chance to incorporate a few modifications that we consider to be meaningful, based on our experience with ERA-Interim. It is true that these modifications lead to a substantial increase in the number of identified trajectories, and in particular there are more rapidly ascending ones compared to the original criteria. We tested the sensitivity of the results of this study to the first of the two modifications,

i.e., to also select very fast ascending trajectories that fulfil the 600-hPa ascent criterion in the first part of the 48-h period and thereafter descend again. Fig. R1 is equivalent to Fig. 5 in the paper, but only includes WCB trajectories according to the Madonna et al. ascent criterion of 600 hPa between times 0 and 48 h (but with the new clustering criterion). Both for all and for the strong WCBs the observed reflectivity and IWC patterns are very similar to those in Fig. 4 in the paper where we used the modified ascent criterion. This is also the case for all other figures shown in the paper. For the second modification no sensitivity study has been done, but also here we expect the sensitivity to be relatively small.

A very detailed comparison between the WCB climatology based on ERA-Interim and ERA5, respectively, is currently done in our group by Katharina Heitmann. She assesses in detail the impact of model differences and the modifications in the WCB identification on the frequency, geographical distribution and characteristics of the WCBs. First preliminary results show that while the modified WCB identification leads to an increase in the frequency of WCBs, the geographical distribution and main characteristics of WCBs are very similar to those documented in Madonna et al. (2014). Since this is work in progress and not the focus of the present study, we prefer not to go into much detail about these technical issues in the present study. Due to the small sensitivity of our results to the exact WCB identification criterion, we regard it as justified to use the slightly modified criteria without discussing the motivation in much detail.

On lines 173-175 we added the sentence "Despite the significant increase in the number of identified WCB trajectories with respect to the original WCB identification criterion, tests have shown that the modifications do not affect the findings of this study."
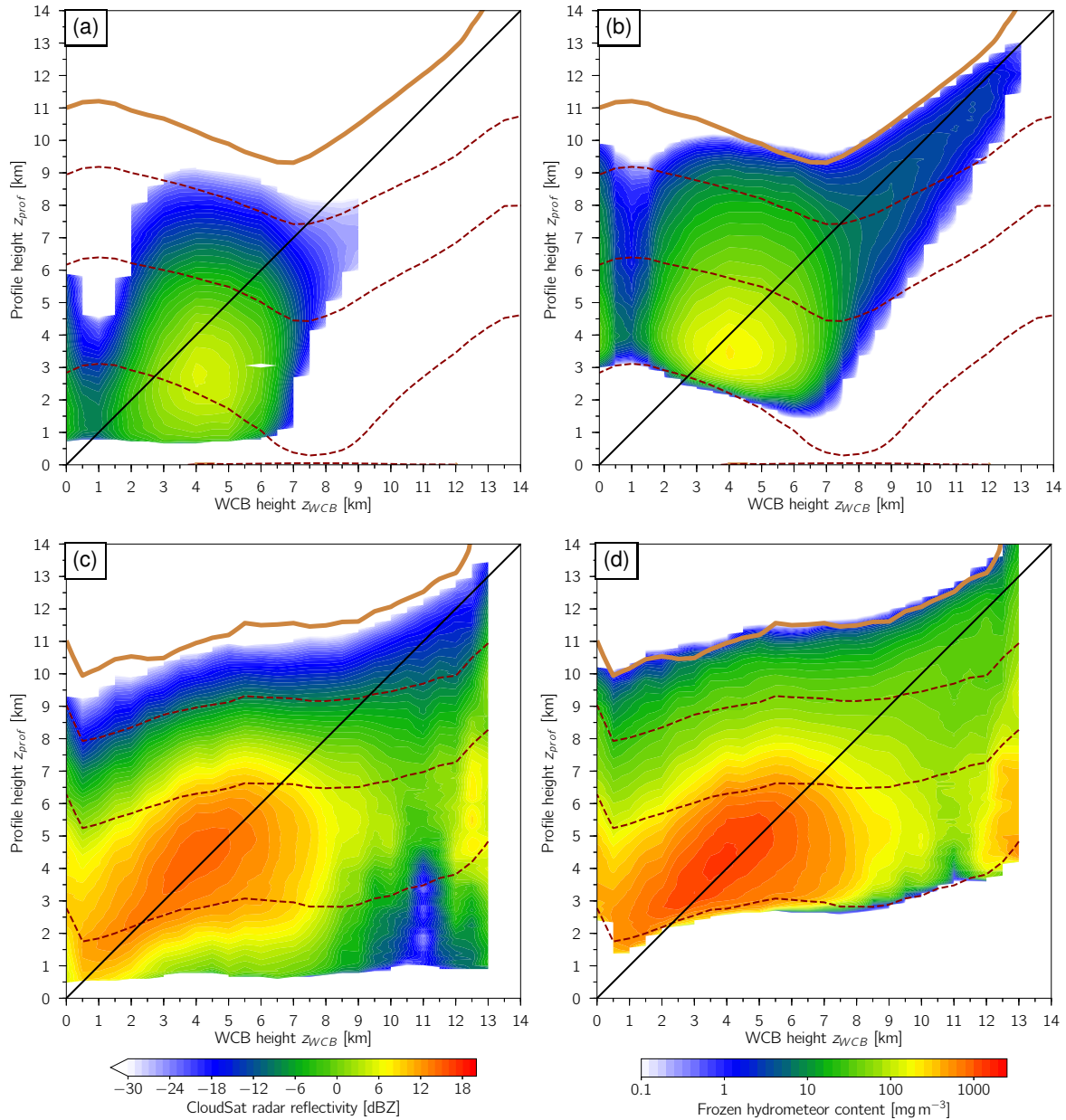
Fig. R1: Equivalent to Fig. 5 in the manuscript, but without considering very fast ascending WCB trajectories that fulfil the 600-hPa ascent criterion in the first part of the 48-h period and thereafter descend again, i.e., when using the original Madonna et al. (2014) selection criteria for WCB trajectories.

Section 2.4: While the matching between WCB trajectories and CloudSat – CALIPSO overpasses is very well explained, I think a schematic of the method could help to visualise it, if feasible. Otherwise, referring to Fig. 1b could already help.

Reply: We now refer to Fig. 1b to illustrate the matching and include a schematic to illustrate how several satellite profiles are attributed to a single matching WCB trajectory in the climatological analysis (see reply below).

L. 179: "the 56 preceding and succeeding profiles" seemed to come out of nowhere the first time I read it. I then understood that 113 profiles times the horizontal resolution of DARDAR

would make 124 km, but at first it is hard to understand the rationale behind these numbers. Maybe it would help the reader to explain where the 56 comes from. This is somehow related to the previous comment. If you include a schematic on the matching, this could be added in it.

Reply: You are right, we now include a schematic to illustrate the method (see Fig. R2 below and Fig. 1 in the revised manuscript) and tried to improve the explanation by slightly changing the sentences as follows:

"In the climatological study, several satellite profiles are attributed to each matching WCB trajectory. They are then averaged to increase the representativity of the observations (see schematic illustration in Fig. 1). In total, 113 satellite profiles are averaged per WCB-match - that is, the profile with the closest distance to the WCB air parcel, plus the 56 preceding and the 56 succeeding profiles. With a distance of 1.1 km between each satellite profile, the 113 assigned profiles correspond to a track segment length of about 124 km …"
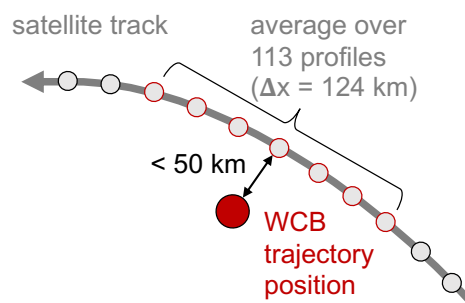

Fig. R2: Schematic illustration of the method to attribute several satellite profiles to a matching ERA5-based WCB trajectory in the climatological analysis.

L. 239-247: I really like how you summarise the end of a section and introduce a new one.

Reply: Thank you!

L.273-275: Do you have a possible explanation for that?

Reply: We are not sure why WCBs with exceptionally strong radar reflectivities in their inflow occur further north than the mean over all matches. We have to leave it for further research to better understand this behaviour.
However, we would like to add one possible hint, which is based on an unpublished earlier analysis. For these older results, Fig. R3 shows horizontal composites of the upper-level PV structure for all and the strong WCBs in the inflow (i.e., for matches below 2.5 km height). The coordinates are defined relative to the position of the matching WCB trajectory, which is relocated to 0° longitude and latitude. Both all and the strong WCBs are located close to the extratropical upper-level waveguide between a trough and a ridge. However, the strong WCBs are located about 5° closer to the waveguide, right at the leading edge of the trough, and the PV gradient associated with the trough is stronger. This suggests that the further northward located inflow in the subcategory of strong WCBs experiences a stronger upper-level forcing for ascent, which could explain the particularly strong radar reflectivities associated with them.

The lower tropopause and accordingly the stronger upper-level forcing for ascent in the subcategory of strong WCBs are also evident in the vertical composites in the manuscript (compare Figs. 6f and 8f). However, this possible explanation is rather speculative, and we prefer not to include it in the paper.
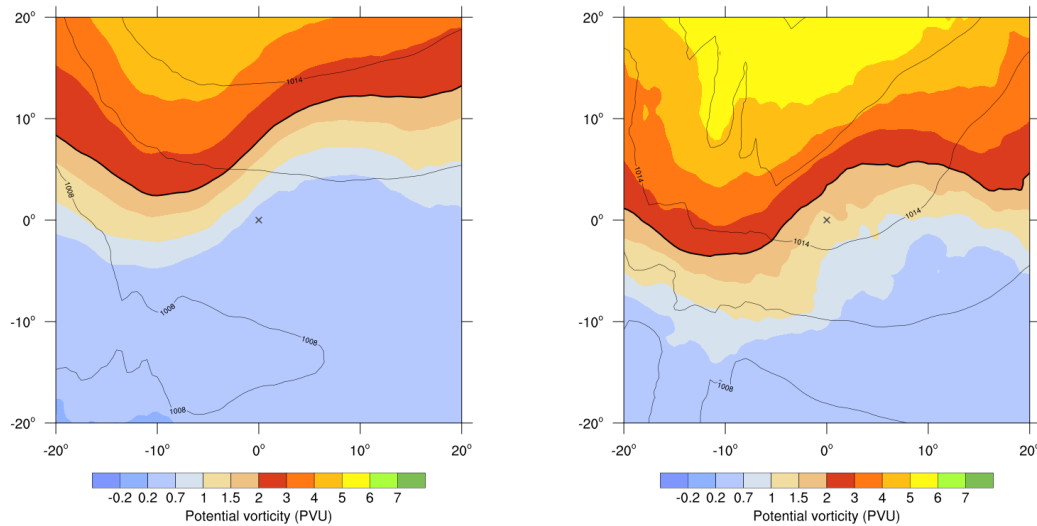

Fig. R3: Composites of PV at 320 K (pvu; shading) and sea level pressure (black contours every 3 hPa) over (left) all WCBs and (right) strong WCBs that are located below 2.5 km height. The black cross at the centre marks the position of the matching WCB trajectories.

L. 363: "[…], and there is no clear indication for a melting layer in the radar signal."
Actually if you look at the shape of the reflectivity contours (Fig. 4c), even if it is mainly oriented along the diagonal, there is a change in the curvature which follows the 0°C isotherm, indicating a secondary maximum of reflectivity. I think this could be an indication of the melting layer in the radar signal. To fully appreciate the melting layer signature at W-band, one has to consider the following: (i) For a ground-based W-band radar there is no bright band as is the case at lower frequencies, instead "an abrupt increase in the radar reflectivity without a following decrease at the base of the melting layer" (Kollias and Albrecht, 2005). (ii) For a nadir-pointing W-band radar (e.g. CloudSat) the bright band occurs du to "an increase in radar reflectivity from the dielectric effect of water, followed by a rapid signal decline [...] caused by correspondingly strong signal attenuation." (Sassen et al. 2007). I think both cases (all WCBs and strong WCBs) nicely correspond to the description of Sassen et al. 2007: we have a maximum of reflectivity followed by a sharp decrease due to attenuation (especially in Fig. 4c, which is consistent with stronger rainfall). It seems that the maximum of reflectivity is not due to the higher dielectric constant of the liquid water coating the melting snowflakes, since it occurs above the 0°C isotherm, but rather to attenuation starting above the melting layer. Hence, it suggests that the attenuation effect is stronger than the dielectric effect. The attenuation starting above the melting layer could be partially explained by the presence of supercooled liquid water droplets (see Fig. 5b and 7b): they are so tiny, that even at W-band they will not significantly contribute to the reflectivity, despite their higher dielectric constant than the surrounding snowflakes. However, they contribute significantly to the attenuation.

Reply: Many thanks for these useful insights, they have greatly helped us to better understand the signal at the melting layer. You are right that the description of Sassen et al. (2007) fits well with the reflectivity signal in the case study (Fig. 3a) and in the composite of strong WCBs (Fig. 5c): There is a first reflectivity maximum above the melting layer in the mixed-phase clouds, followed by a dim band at the top of the melting layer that is most likely due to snowfall attenuation. Below the melting level, a second increase in the signal is present that is probably caused by the dielectric effect of water, followed by a rapid signal decline due to rainfall attenuation.

In the revised manuscript, we briefly discuss the dim band in the case study on lines 223-227, and in the climatological part we deleted the words "and there is no clear indication for a melting layer in the radar signal" and now write instead that "the signal decrease below the WCB indicates strong snow and rain attenuation" (line 388).

L. 434: Even above zWCB=9km I see no gap between the frozen and liquid hydrometeors. Do I interpret this correctly?

Reply: You are right, thank you for pointing this out. We changed the sentence to "In contrast to all WCB matches, there is no gap between the frozen and liquid hydrometeors throughout the inflow, ascent and outflow (Fig. 7a,b), consistent with the higher RH_{ice} (Fig. 7c)."

Figure 2/5/7: Maybe it could be recalled in the caption that IWCDARDAR includes SWC and hence IWCDARDAR should be compared to IWCERA5 + SWCERA5. For a reader comparing Fig. 5 and 4 without reading Sect. 4.1, this could be confusing.

Reply: Thank you for pointing this out, we now mention it explicitly in the captions of Fig. 3, 5 and 6. Furthermore, in each figure we changed the title of the label bar from "IWC" or "IWC + SWC" to "Frozen hydrometeor content", to make it clearer that IWC + SWC from ERA5 should be compared to IWCDARDAR.

Figure 4c: There is a nice secondary maximum of reflectivity for zWCB> 12 km and zprof between 3 and 7 km. This is probably associated with the subtropical convective system mentioned in Sect. 4.1. It is also well depicted in Fig. 7a,b and seem to correspond to negative moist static stability (Fig. 7e). Even if subtropical systems are not the focus of this study, it could be mentioned, since it
is a rather interesting feature.

Reply: It is true, this is an interesting feature as well, which has also been mentioned by reviewer 2. We now mention it on lines 391-393 and 474-478.

Technical corrections

L. 61: According to WCD guidelines, footnotes should be avoided. I personally find it OK, it is just for you to know in case.

Reply: Thanks, we now incorporate the footnotes in the main text.

L. 92: According to WCD guidelines, Section should be abbreviated Sect. in running text, this should be corrected throughout the manuscript.

Reply: Thanks, we changed it everywhere.

L. 175: Suggestion: "A match between a WCB trajectory position and the satellites' track [..]" would be maybe more precise.

Reply: You are right, thank you, we changed it as you suggested.

L. 214: Suggestion: "[…], the lower reflectivity and IWC values suggest ice clouds rather than falling snow." would be more appropriate than "indicate".

Reply: Thank you, we replaced "indicate" by "suggest".

L. 225: "The IWC values strongly increase [...]" would be more precise than "The values strongly increase [...]"

Reply: Thank you for pointing this out, it is true that we should be more precise here. It is the sum over the IWC and SWC values that strongly increases toward the melting layer, so we changed the sentence as follows: "The sum over the ice and snow values strongly increases toward the melting layer and peaks right above the melting layer in the deep frontal clouds, where most of it is present as falling snow (see thin black contours in Fig. 3d)."

L. 226: "[…] (see grey contours)." You mean the thin black contours of SWC in Fig. 2d?

Reply: You are right, we meant the thin black contours, we changed it accordingly (see comment above).

L. 193, 245, 372: I am not sure if the capitalisation of "Section" is correct if it does not refer to a specific section (i.e. followed by a number)? To be checked.

Reply: Thank you, we leave this to the copy editor.

L.413: you probably mean Fig. 5b.

Reply: Yes, thank you for spotting this typo.

L. 445: "In the WCB outflow, the PV values are anomalously low PV (< 0.2 pvu)." The second "PV" seems not necessary.

Reply: You are right, thank you.

L. 569: Just in case, this article is now in final form in ACP: https://doi.org/10.5194/acp-20-7373-2020

Reply: Thank you, we changed it accordingly.

Figure 6: Why not using the same colour for all WCBs and strong WCBs as in Fig. 3d or the opposite?

Reply: Good point, we changed the colours in Fig. 3d, they are now as in Fig. 6.

Reviewer 2 (Derek Posselt)

Summary: *This paper uses retrievals of ice water content from CloudSat and CALIPSO to study the properties of warm conveyor belts, and to evaluate the clouds produced by the ERA5 reanalysis. The authors analyze a representative WCB case, then extend their analysis to multiple years of observations, producing composites of retrieved ice water content for all WCBs and for the 5% corresponding to the largest radar reflectivity values. They find interesting signals in the observations that indicate a connection between WCB properties and the vertical distribution of ice cloud content. They further connect the ice cloud properties to dynamics and thermodynamic properties by analyzing the static stability and PV in the reanalysis data. The paper is well conceived and well written, and I have only minor comments and suggestions for the authors. I begin with a few general comments, then itemize a number of specific comments after.*

General Comments:

1. One must be careful, when comparing model output to satellite retrievals, to note where there may be overlap between the sources of data. In the case of DARDAR ice water content retrievals, the ice cloud estimates depend on temperature profiles that are obtained from ECMWF. As such, the IWC information in the retrievals is not entirely independent of the model that is being evaluated. This does not mean that the comparison is not valid, but I would suggest that the authors note the fact that there is information from ECMWF in the DARDAR product and perhaps discuss how this might affect the conclusions drawn in the study.

Reply: You are right, it is important to point out that the two datasets are not entirely independent, thank you for this comment. In particular, the use of temperature profiles from ECMWF analyses most likely explains the good agreement of the melting layer height in the satellite retrievals and ERA5, i.e., a good anchoring at the melting layer (Fig. 3c, 5b,d).
We now mention and discuss this on lines 121-123, 238-243 and 533-537.

2. There appears to be a convective (vs stratiform) signal present for strong WCBs with heights above 12 km (see my specific comments below for details). I wonder if it would be of interest to the authors to add a brief discussion of this?

Reply: We agree that there appears to be a convective signal, and it is most likely related to subtropical cyclones, because matches with strong WCBs at $z_{WCB} > 12$ km occur in the subtropics, at about 15-30°N (see blue line in Fig. 4d). We didn't include a discussion of it in the previous draft, as subtropical convective systems are not the focus of our study. But it is true that it is nevertheless an interesting feature that has also been noted by the other reviewer. We now include a brief discussion of it on lines 391-393 and 474-478.

3. One question that comes to mind in any observation-based study (and in an evaluation of model output in particular) is the degree to which observations are able to characterize processes. The authors have done a nice job inferring the connection between satellite retrievals and processes via the analysis of PV and the thermodynamic environment. However, the A-Train sees only snapshots of cloud fields and (as the authors point out) rarely revisits a given storm more than once in its life cycle. Looking toward the future, I wonder what is missing from the observations that would enable a more specific process-based analysis and model evaluation? What are the most critical observational needs for improving the understanding of the time evolution of storms? Will the addition of vertical motion estimates (e.g., from the doppler radar on EarthCARE) be helpful, or are time resolved measurements of the interior of the WCB clouds necessary? The paper is complete with or without this discussion, but I wonder if the authors would like to comment (given their expertise in this area) on what would be most useful in their future analyses?

Reply: This is a very interesting question. As you point out, the vertical motion estimates from the Doppler radar on the EarthCare satellite will certainly be very valuable to characterize the dynamical processes associated with WCBs in further detail, and to evaluate them in model data. Also, a higher spatial coverage would be useful, such that the temporal evolution of the satellite measurements along individual WCB trajectories could be investigated. While a full coverage will certainly not be feasible in the near future, the increase in the spatial coverage of radar and lidar data with the launch of the EarthCare satellite will already enable a more in-depth study of the time evolution of the WCBs and the associated cyclones.
As discussed in the ECMWF newsletter article of Rodwell et al. (2018), it is also important to accurately initialise humidity in models to improve the representation of WCBs, but it is challenging to do so. For instance, in cloudy regions such as WCBs, there is a lack of humidity measurements, as radiosondes are scarce, and water vapour lidars are strongly attenuated in clouds. Observational data of water vapor in cloudy regions would be very valuable for a better understanding of the cloud processes in WCBs.

Specific Comments:

1. P6, line 173. Is it true that the satellite observations are available more often than hourly? Even over the poles, the data is available only approximately once every 100 minutes, with longer delays with decreasing latitude. I wonder if you meant that the satellite intersections of WCBs often happen between the 1-hour analysis intervals?

Reply: We apologize, this was not well explained in the manuscript. It is true that the temporal resolution of the satellite data at one location is very low, with a repeat cycle of 16 days. However, we would like to say that the individual satellite profiles are available every about

0.16 seconds (without referring to a specific location) and therefore much more often than the hourly ERA5 data. We reformulated this on lines 181-182.

2. P8, lines 227-229. What is the uncertainty in the DARDAR IWC retrieval? Is there a known issue with retrieval of ice in mixed phase regions in DARDAR? I wonder whether the differences between ERA-5 and DARDAR are within the 1-sigma uncertainty of the observations? The same question would apply to the composite comparisons in section 4.

Reply: Figure R4 shows for the case study the DARDAR-retrieved IWC (same as Fig. 3e in the paper) and the associated uncertainty in a running mean over 113 satellite profiles. The uncertainties are expressed as one standard deviation percentage errors in the natural logarithm of the IWC. For instance, an uncertainty of 50% for an IWC value of 2 mg m^{-3} implies that the value ranges between 2 mg m^{-3} / 1.5 and 2 mg m^{-3} x 1.5 (for details see Eliasson et al. 2013: Systematic and random errors between collocated satellite ice water path observations. J. Geophys. Res.)
The uncertainties are about 20-30% in the pure ice clouds at upper levels, where the IWC values are low. Between the -20°C isotherm and the melting layer, where the IWC values are high and presumably associated with mixed-phase clouds, the uncertainties range from 5-20% near -20°C and 10-40% near the melting layer. Even with uncertainties of 40%, the difference between the maximum IWC values in the observations (1640 mg m^{-3}) and ERA5 (1050 mg m^{-3}) are larger than the one-sigma uncertainty range of the observations. This is also the case for the composite comparison, where the uncertainties are significantly lower than in the case study because of the averaging over a large number of satellite profiles (see reply to question 5).
We do not know of an issue with the retrieval of ice in the mixed-phase region in DARDAR. However, the patterns in Figs. R4b and R6b,d (see reply to question 5) indicate that the uncertainties are indeed highest in the lower part of the mixed-phase clouds near the melting layer.

We now include a discussion of the uncertainties in the DARDAR-retrieved IWC on lines 130-133, 249-252, 408-413 and 461-464.
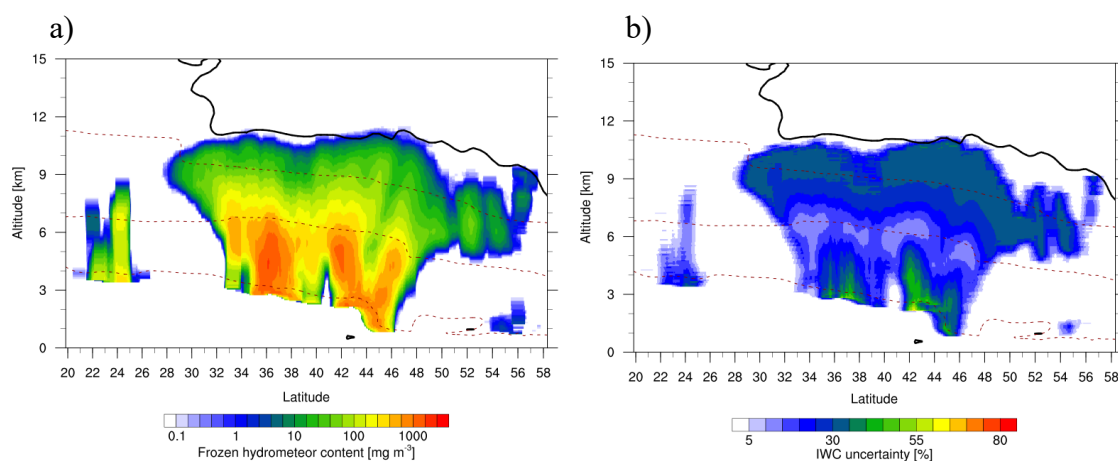

Fig. R4: Vertical cross section along a North Pacific WCB at 00 UTC 3 January 2014 of (a) the DARDAR-retrieved IWC (mg m^{-3}; shading) and (b) the associated percentage uncertainty (%; shading) in a running mean along 113 satellite profiles, together with the ERA5-based temperature (red dashed contours at 0°, -20° and -40°C) and the 2-pvu contour (thick black line). (a) is equivalent to Fig. 3e in the paper.

3. P8, lines 249-250. In Figs 3a and 3b, I noticed an apparent gap in the concentration of WCBs (in the full set and also the "strong" subset) around 170 W longitude and extending through all latitudes from SE to NW. It looks like there may be data missing along a satellite swath? I am curious as to whether this is a real (geophysical) feature or an artifact in the data?

Reply: Thank you very much for noting this gap, there was indeed data missing along the satellite swath. We found the source of the problem and incorporated the missing data in the analysis. We updated all climatological figures, redid the analysis for the category of strong WCBs and changed the text accordingly. Compared to the previous version, the number of matches has increased from 502'977 to 509'042. This relatively small increase has almost no impact on the results and the updated figures are very similar to those in the previous version, such that incorporation of the previously missing data does not affect the findings of this study.

Note that in the updated Fig. 4a there is still an apparent gap around 165°W along a narrow region. Figure R5 shows the number of satellite profiles at each grid point that have been taken into account in the present study, together with the climatological WCB trajectory frequency for winter 2006 to 2016, i.e., for the considered years (the WCB trajectory frequency slightly differs from the one shown in Fig. 4a in the paper, where all years between 1980 and 2018 have been taken into account). The satellite data does not show any gaps, and also the WCB trajectory frequency is high around 165°W. This suggests that the apparent gap around 165°W in Fig. 4a is not an artefact of the data, but that by chance the number of WCB trajectories present in this region was slightly reduced during the satellite overpasses.
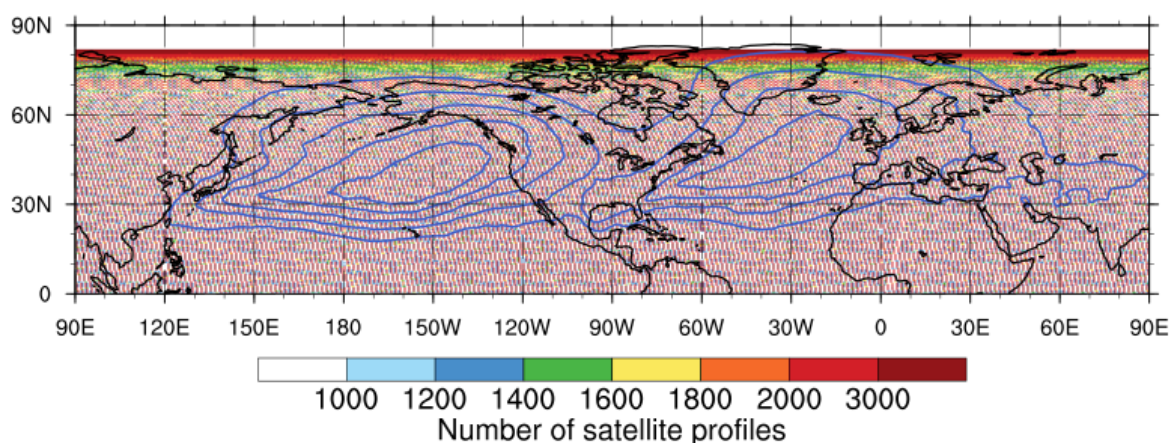

Fig. R5: Spatial distribution of the satellite profiles taken into account in the present study (shading). The colours show the number of profiles in each 0.5° bin. Overlaid is the ERA5-based climatological frequency of WCB trajectories for December-February 2006-2016, i.e., for the years considered in this study (blue contours every 10%). Note that the WCB trajectory frequency slightly differs from the one in Fig. 4a,b, which is shown for December-February 1980-2018.

4. P11, lines 354-355. It is interesting that there are large reflectivities (and relatively warm columns) where the "strong" WCB heights are greater than 12 km. As the authors point out, it is not possible from Figs. 4c and 4d to determine trajectories; however, I

wonder if the fact that the mean profiles extend through the depth of the troposphere with high reflectivities and warm temperatures indicate convective (vs stratiform) profiles?

Reply: We agree that this is most likely a convective signal, and we now discuss it briefly on lines 391-393 and 474-478 (see also reply to the general comment 2).

5. P12, lines 377-378. I have the same question here as I did in for the case study - how do the obs-model differences compare with the observational uncertainty? In this case, would one expect the observation uncertainty to be smaller than for the individual case (since the results consist of an average over a large number of profiles)?

Reply: Figure R6 shows for all and the strong WCBs vertical composites of the percentage error of the IWC retrievals, separately for different WCB heights. Hereby, the mean error at each profile position has been divided by $\sqrt{N}$, i.e., the square root of the number of WCB matches in the respective WCB height bin (see histogram in Fig. 4c in the manuscript for the number of matches N per WCB height). The observational error is therefore indeed much smaller than in the case study (cf. Fig. R4b).

For the entire climatology, the percentage error is particularly low, with values between 0.025% and 0.17% up to about $z_{WCB} \sim 12$ km, and slightly larger values of up to 1.7% for z_{WCB} > 12 km (Fig. R6b). The larger errors at z_{WCB} > 12 km are due to the much lower number of matches at this height (see histogram in Fig. 4c in the manuscript). At lower z_{WCB}, the error pattern strongly resembles the IWC pattern in Fig. R6a, with maximum errors of 0.17% at z_{WCB} = 3.5-4 km and z_{prof} = 3.5-4 km coinciding with the satellite-retrieved IWC maximum of 260 mg m^{-3} (Fig. R6a). Thus, the error range is 260 mg m^{-3} +/- 0.17%, i.e., the one-sigma uncertainty lies between 260 / 1.0017 = 259.6 mg m^{-3} and 260 x 1.0017 = 260.4 mg m^{-3}. The ERA5-based maximum IWC values of 160 mg m^{-3} are therefore significantly lower than the one-sigma percentage uncertainty of the observations, i.e., the conclusions in this study are valid.

In the category of strong WCBs, the errors are larger than for the entire climatology because of the smaller number of matches, but they are still significantly smaller than in the case study (Fig. R6d). For z_{WCB} between ~0.5 and 12 km height, the error pattern again coincides approximately with the IWC pattern (Fig. R6c), with maximum values of 1-1.25% around the IWC maximum between the melting layer and the -20°C isotherm, and slightly lower values at higher altitudes. Hence, also for the category of strong WCBs the differences between the peak DARDAR-retrieved IWC values (1180 mg m^{-3}) and ERA5 (540 mg m^{-3}) are significantly larger than the one-sigma uncertainty range of the observations.

We now include a discussion of the uncertainties in the DARDAR-retrieved IWC on lines 130-133, 249-252, 408-413 and 461-464.
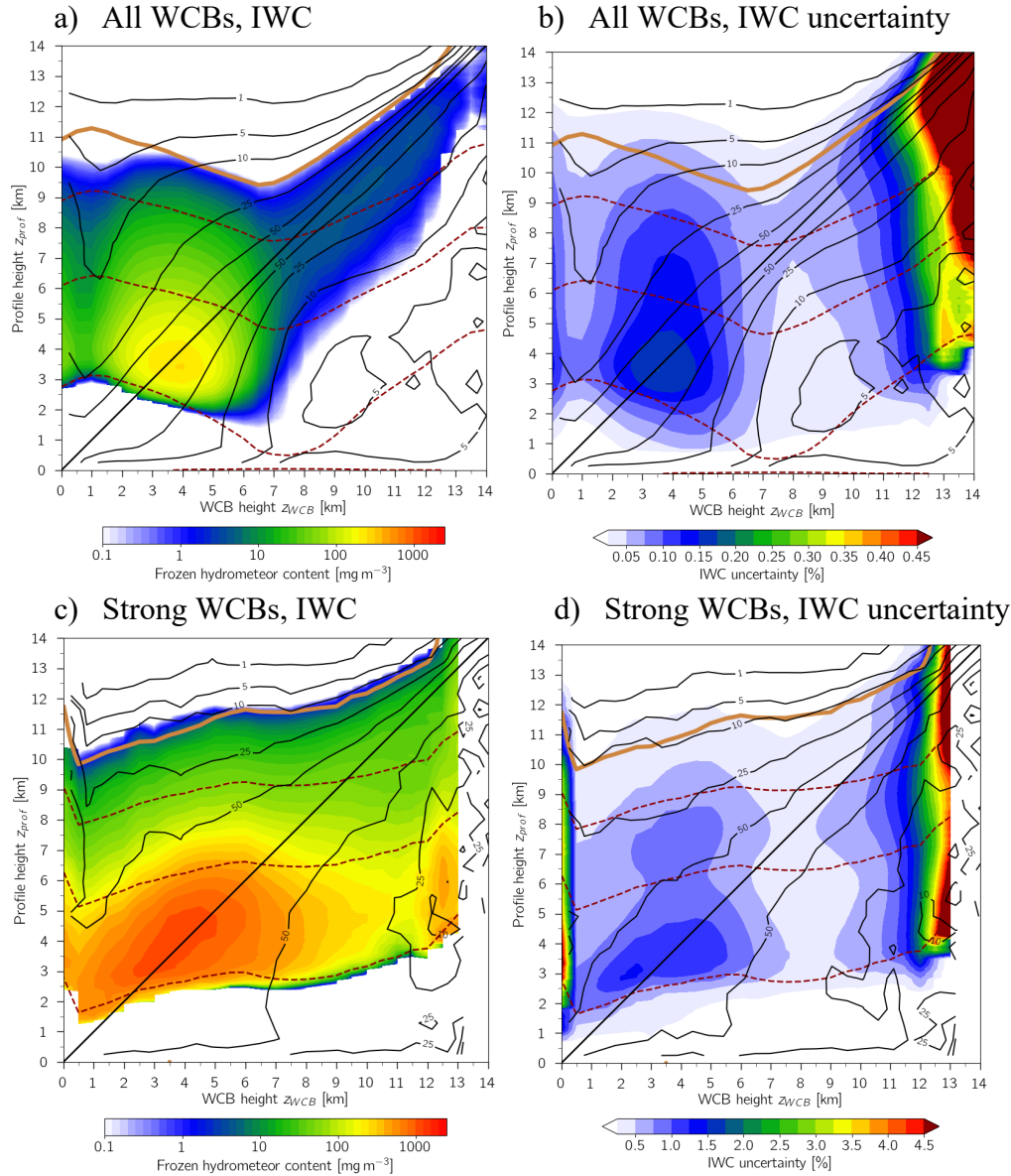
Fig. R6: Composites of (a, c) the DARDAR-retrieved IWC (mg m^{-3}; shading) and (b, d) the associated percentage uncertainty (%; shading), separately for different height bins of the matching WCB air parcels. The composites are shown for all WCBs in the top panels and for the strong WCBs in the bottom panels. The black lines show the relative WCB trajectory frequency at each profile height (contours at 1, 5, 10, 25, 50 and 100%), the red dashed line the temperature (contours at 0°, -20° and -40°C), and the brown line the 2-pvu contour, all three fields interpolated from ERA5. (a) and (c) are equivalent to Figs. 5b and 5d in the paper.

6. P14, lines 425ff. As noted above in my comment on the deep portions of strong WCBs in Fig. 4c, the thermodynamic analysis appears to support the presence of convective clouds for WCB trajectory heights above 11 km. There is a strong uptick in precipitation rate (including convective) (Fig. 6) as well as high RH through the depth of the troposphere (Fig. 7c), high theta-e values (Fig 7d), and weak stratification (Fig 7e).

Reply: It is true that the thermodynamic analysis supports the presence of convection below the WCB outflow at z_{WCB}> ~12 km, and we now discuss it briefly on lines 391-393 and 474-478 (see also reply to the general comment 2).

Vertical cloud structure of warm conveyor belts – a comparison and evaluation of ERA5 reanalyses, CloudSat and CALIPSO data

Hanin Binder[1], Maxi Boettcher[1], Hanna Joos[1], Michael Sprenger[1], and Heini Wernli[1]

[1]Institute for Atmospheric and Climate Science, ETH Zurich, 8092 Zurich, Switzerland

Correspondence: Hanin Binder (hanin.binder@env.ethz.ch)

Abstract. Warm conveyor belts (WCBs) are important cyclone-related airstreams that are responsible for most of the cloud and precipitation formation in the extratropics. They can also substantially influence the dynamics of the cyclone and the upper-level flow. So far, most knowledge about WCBs is based on model data from analyses, reanalyses and forecast data, with only a few observational studies available. The aim of this work is to gain a detailed observational perspective on the vertical cloud and precipitation structure of WCBs during their inflow, ascent and outflow, and to evaluate their representation in the new ERA5 reanalysis dataset. To this end, satellite observations from the CloudSat radar and the CALIPSO lidar are combined with an ERA5-based WCB climatology for nine Northern Hemisphere winters. Based on a case study and a composite analysis, the main findings can be summarised as follows: (i) WCB air masses are part of deep, strongly precipitating clouds, with cloud-top heights at 9-10 km during their ascent, and an about 2-3 km deep layer with supercooled liquid water co-existing with ice above the melting layer. The maximum surface precipitation occurs when the WCB is at about 2-4 km height. (ii) Convective clouds can be observed above the inflow and during the ascent. (iii) At upper levels, the WCB outflow is typically located near the top of a 3 km deep cirrus layer. (iv) There is a large variability between WCBs in terms of cloud structure, peak reflectivity, and associated surface precipitation. (v) The WCB trajectories with the highest radar reflectivities are mainly located over the North Atlantic and North Pacific, and – apart from the inflow – they occur at relatively low latitudes. They are associated with particularly deep and strongly precipitating clouds that occur not only during the ascent, but also in the inflow and outflow regions. (vi) ERA5 represents the WCB clouds remarkably well in terms of position, thermodynamic phase and frozen hydrometeor distribution, although it underestimates the high ice and snow values in the mixed-phase clouds near the melting layer. (vii) In the lower troposphere, high potential vorticity is diabatically produced along the WCB in areas with high reflectivities and hydrometeor contents, and at upper levels, low potential vorticity prevails in the cirrus layer in the WCB outflow. The study provides important observational insight into the internal cloud structure of WCBs, and emphasises the ability of ERA5 to essentially capture the observed pattern, but also reveals many small- and mesoscale structures observed by the remote sensing instruments but not captured by ERA5.

1 Introduction

Extratropical cyclones are typically associated with well-defined moist ascending airstreams referred to as warm conveyor belts (WCBs; e.g., Harrold, 1973; Carlson, 1980; Wernli and Davies, 1997). WCBs are responsible for most of the cloud and pre-

cipitation formation and poleward energy transport in extratropical cyclones (Browning, 1990), and thereby they play a crucial role for the hydrological cycle and the Earth's energy balance. WCBs are also essential from an atmospheric dynamical point of view. The intense cloud-diabatic processes within the ascending airstreams lead to potential vorticity (PV) modifications in the lower and upper troposphere, which can intensify the associated cyclone

30 ~~(Binder et al., 2016)~~ (Davis and Emanuel, 1991; Rossa et al., 2000; Binder et al., 2016) and influence the synoptic- and large-scale flow at the tropopause and the downstream weather evolution (e.g., Wernli and Davies, 1997; Grams et al., 2011).

Because of the crucial role of WCBs for many atmospheric processes, it is important to accurately represent them and the associated clouds and precipitation in numerical weather prediction and climate models. Several studies indicated that errors in their representation can lead to forecast errors of the weather downstream (e.g., Gray et al., 2014; Martínez-Alvarado and

35 Plant, 2014; Madonna et al., 2015; Grams et al., 2018). For instance, it has been shown that cloud-microphysical processes in WCBs (Joos and Wernli, 2012; Joos and Forbes, 2016) and the initial moisture distribution in the WCB inflow (Schäfler et al., 2011; Schäfler and Harnisch, 2015) play a crucial role for the meso- and large-scale flow evolution. However, diabatic processes are difficult to represent in global models because they typically occur on smaller scales than the model resolution and must therefore be parameterised. Additionally, the understanding of many physical processes occurring in warm-, ice- and

40 particularly mixed-phase clouds is still incomplete (e.g., Illingworth et al., 2007; Joos and Forbes, 2016). This highlights the importance to complement our knowledge about WCBs and the embedded small-scale processes, which is mainly based on numerical model data, with observational studies.

Only a few observational studies exist on WCBs. Schäfler et al. (2011) compared lidar humidity observations of a sum-mertime WCB over southwestern Europe with analysis data from the European Centre for Medium-Range Weather Forecasts

45 (ECMWF) and revealed significant deficiencies in the model's representation of the low-level moisture in the WCB inflow region. Crespo and Posselt (2016) analysed a WCB over the North Atlantic that was sampled several times by remote sensing instrumentation. They documented a clear transition from a stratiform to a convective cloud structure during the evolution of the cyclone. The distinction between mesoscale, slantwise ascent of the WCB and upright embedded convection had already been made in 1993 in a study on the mesoscale frontal structure of an explosively intensifying cyclone measured during the ER-

50 ICA field experiment (Neiman et al., 1993). Embedded deep convection was also documented in a number of WCBs observed in the Mediterranean region (Flaounas et al., 2016, 2018) ~~,~~ and during the NAWDEX field experiment in the North Atlantic ~~(Oertel et al., 2019)~~(Oertel et al., 2019; Blanchard et al., 2020). While slantwise WCB ascent leads to large-scale stratiform precipitation and the formation of widespread regions with low-PV air at upper levels, convective WCB ascent goes along with peaks of particularly strong surface precipitation and the formation of mesoscale upper-level PV dipoles, including regions with

55 negative PV (Oertel et al., 2020). Finally, Gehring et al. (2020) investigated the snowfall microphysical processes in a strongly precipitating wintertime WCB over the Korean Peninsula that was observed with radar data, radio soundings and snowflake photographs. They showed how the WCB created ideal conditions for rapid precipitation growth, including the formation of supercooled liquid water in the strongly ascending air masses, which favoured intense riming and aggregation.

Many cloud processes, for example radiative heating or cooling of the atmosphere, condensational processes and the effi-

60 ciency of precipitation production, crucially depend on the vertical structure and distribution of clouds (e.g. Posselt et al., 2008).

With the launch of the CloudSat radar (Stephens et al., 2002, 2008) and the ~~CALIPSO~~[1] Cloud-Aerosol Lidar and Infrared Pathfinder Satellite Observation (CALIPSO) lidar (Winker et al., 2003, 2009) in April 2006, high-resolution global measurements of the vertical structure and properties of clouds, precipitation and aerosols have become available. The satellites are part of the NASA's Afternoon Train (A-Train), a constellation of satellites that travels in close formation in a sun-synchronous orbit, allowing for near-simultaneous measurements of various key parameters that affect the Earth's weather and climate. Studies based on CloudSat and CALIPSO measurements have provided invaluable insight into the distribution of clouds and precipitation in extratropical cyclones, and the associated complex dynamical and physical processes. Posselt et al. (2008) compared the frontal clouds observed by CloudSat along a warm, a cold and an occluded front, respectively, with those described in the Norwegian polar-front model (Bjerknes and Solberg, 1922). While the historical description and the modern observations reveal remarkable similarities, CloudSat provides a detailed view of the internal cloud structure, thereby adding a new component to the classical conceptual model. Vertical composites of frontal clouds based on CloudSat and CALIPSO data (Naud et al., 2010, 2012, 2014, 2015) also revealed some similarities to the historical model, but even more to the conveyor belt model and specifically the WCB, with mid- and high-level clouds typically occurring to the east of the cold front and above the warm front. Field et al. (2011) combined observations from CloudSat and passive sensors to create three-dimensional composites of the cloud and precipitation structure in extratropical cyclones, and also used these to evaluate the representation of clouds and precipitation in a numerical model. CloudSat and CALIPSO observations have also been used to validate the global ice cloud representation in several versions of the ECMWF and UK Met Office models with different ice cloud parameterisations (Delanoë et al., 2011). It was found that the models generally reproduce the main geographical and temperature-dependent distributions, although with some deficiencies, and that the representation is considerably improved in schemes with prognostic variables for cloud ice, snow, liquid water and rain compared to schemes with diagnostic formulations for precipitation and mixed-phase clouds.

The objective of this study is to gain an observational view on a large number of WCBs in Northern Hemisphere winter, and to evaluate their representation in the new ERA5 reanalyses. For this, we combine satellite observations from CloudSat and CALIPSO with a WCB climatology compiled with ERA5. Specifically, the aims are to (i) use observational data to characterise the vertical cloud and precipitation structure of WCBs during their inflow, ascent and outflow in terms of vertical extent, radar reflectivity and ice water content, (ii) gain insight into the ERA5-based meteorological environment of the observed WCBs in terms of saturation, static stability and PV, (iii) quantify differences in the cloud structure and the meteorological environment between typical WCBs and WCBs with particularly high radar reflectivities, and (iv) assess the ability of ERA5 to represent ice and snow in WCB clouds in comparison to CloudSat and CALIPSO.

The remainder of the paper is organised as follows. Section 2 describes the satellite measurements and ERA5 reanalyses, as well as the method to combine the two datasets. In ~~Section~~Sect. 3 we look at the cloud structure of an exemplary WCB in the North Pacific that was measured by the A-Train at the time of strongest intensity of the associated cyclone. The climatological analysis of the vertical cloud structure of WCBs is presented in ~~Section~~Sect. 4, and a summary and discussion of the results are provided in ~~Section~~Sect. 5.

---

[1] ~~Cloud-Aerosol Lidar and Infrared Pathfinder Satellite Observation~~

2 Data and Methods

To characterise the vertical cloud and precipitation structure of the WCBs, and to gain insight into the meteorological environment they are embedded in, satellite observations from the CloudSat radar and the CALIPSO lidar are combined with ~~ERA5-reanalyses~~ ERA5 reanalyses from the ECMWF. The period chosen for the study extends from December 2006 to the end of January 2016, and the analysis is confined to Northern Hemisphere winter (December-February). Winter 2011/2012 is excluded from the study, as CloudSat was not part of the A-Train during that time period.

2.1 Satellite observations

Reflectivity profiles from the Cloud Profiling Radar (CPR) onboard the polar-orbiting CloudSat satellite (Stephens et al., 2002, 2008; Tanelli et al., 2008) are used. The CPR is a nadir-pointing radar operating with a frequency of 94 GHz ($\sim$ 3 mm, W-band). It provides cloud information with a vertical resolution of 485 m (oversampled to produce an effective resolution of 240 m) between the surface and 30 km altitude. The horizontal resolution is about 1.7 km in along-track direction (resulting from a pulse integration period of 0.16 s), and 1.4 km in cross-track direction. In the present study, we use CloudSat reflectivity data provided by the raDAR/liDAR (DARDAR) project (Delanoë and Hogan, 2010, see below), which is interpolated to a grid with 1.1 km horizontal and 60 m vertical resolution. The ~~sensitivity~~ minimum detectable signal of the CPR ~~ranges from~~ is -30~~to 50~~ dBZ. Absorption ~~by gases, liquid water and precipitating particles~~ mainly by liquid water results in a two-way attenuation of the radar signal, which can amount to more than 10 dBZ km^{-1} ~~with high liquid water contents and even~~ below the melting layer and even lead to a full attenuation of the radar signal in strongly precipitating systems (Mace et al., 2007; Marchand et al., 2008). Reflectivity values between about -30 dBZ and -15 dBZ typically represent non-precipitating clouds, values between -15 dBZ and 0 dBZ drizzle or light rain, and values greater than 0 dBZ rain with increasing intensity (Stephens and Haynes, 2007; Haynes et al., 2009). According to Haynes et al. (2009), unattenuated near-surface reflectivity values of more than 0 dBZ (-5 dBZ) are almost certainly associated with significant surface rain (snow) rates of at least 0.03 mm h^{-1}. Radar signals likely contaminated by surface or clear air clutter are filtered out in the present analysis with the CloudSat cloud mask from the 2B-GEOPROF product (Marchand et al., 2008). The effect of surface clutter is most pronounced below 1.2 km height (Marchand et al., 2008), which reduces the ability to investigate the cloud structure at the height of the WCB inflow.

Ice water content (IWC) profiles are obtained from the DARDAR cloud product, version v1 (Delanoë and Hogan, 2010). They are derived using a variational method that combines CloudSat radar reflectivities, CALIPSO lidar attenuated backscatter and infrared radiometer data of the Moderate Resolution Imaging Spectroradiometer (MODIS) on-board the Aqua satellite (for details see Delanoë and Hogan, 2008, 2010). ~~CloudSat~~ In addition, the ice cloud estimates depend on thermodynamic variables like temperature, pressure and specific humidity from the "ECMWF-AUX" dataset, which contains ECMWF variables interpolated to the CloudSat radar bin. The CloudSat and CALIPSO products used to derive the IWC data are highly complementary and sensitive to very different powers of particle size. The radar is able to measure and penetrate optically thick clouds, but it cannot detect optically thin clouds with a reflectivity value below the minimum detectable signal of the radar (-30 dBZ). On the other hand, the lidar is sensitive to optically thin clouds, but it is strongly attenuated in optically thick clouds. Therefore, by linking

CloudSat, CALIPSO and other A-Train measurements, DARDAR combines the advantages of the different sensors, thereby providing a more detailed picture of the structure and microphysical properties of the hydrometeors than could be obtained by

130   the individual sensors. The IWC retrievals consist of the entire frozen hydrometeor fraction, without distinction between small ice crystals and sedimenting snow flakes. ~~Uncertainties in IWC are estimated to~~ For each IWC value the associated uncertainty is estimated. Uncertainties can arise, for instance, from instrumental and measurement errors of the satellites, differences in the radar and lidar footprints, and errors associated with assumptions used in the variational scheme. They are expressed as one standard deviation percentage errors in the natural logarithm of the IWC and can reach up to about 60%. Despite these

135   significant uncertainties, the DARDAR cloud product currently comprises one of the most accurate ~~estimate~~ estimates of ice clouds properties (Stein et al., 2011; Eliasson et al., 2013). Like the reflectivity profiles, the IWC data is available on a grid with 1.1 km horizontal and 60 m vertical resolution.

2.2 ERA5 reanalyses

ERA5 reanalyses from the ECMWF ~~(Hersbach et al., 2019)~~ (Hersbach et al., 2020) are used for the WCB identification and

140   the characterisation of the meteorological environment. ERA5 is based on the Integrated Forecast System model version cycle 41r2 that was operational in 2016. The reanalyses have a spectral resolution of T639 (corresponding to $\sim$31 km) on 137 vertical levels and a temporal resolution of 1 h. In this study, the fields are interpolated to a regular grid with $0.5°$ horizontal resolution.

In ERA5, the parameterization of stratiform clouds and large-scale precipitation is based on an advanced version of the scheme developed by Tiedtke (1993) and includes prognostic variables for water vapour, cloud liquid water, cloud ice, rain,

145   snow and grid box fractional cloud cover (ECMWF, 2016; see also Forbes and Ahlgrimm, 2014). Interactions between the various water species are described with parameterisations for condensation, deposition and freezing via stratiform and convective processes, evaporation, sublimation and melting, as well as the generation of precipitation via autoconversion, accretion and snow riming. Precipitating particles have a terminal fall speed and can be advected between grid boxes by the three-dimensional wind. Supercooled liquid water can exist at temperatures between $0°C$ and the homogeneous freezing threshold

150   at $-38°C$. When ice and supercooled liquid co-exist, the ice crystals grow at the expense of the liquid water droplets via the Wegener-Bergeron-Findeisen mechanism. Convection is parameterised by a bulk mass flux scheme based on Tiedtke (1989), with a modified convective available potential energy closure (Bechtold et al., 2014). It considers deep, shallow and midlevel convection. The collective behaviour of a range of cumulus clouds in a grid cell is represented by a single pair of plumes describing the updraft and downdraft mass fluxes associated with the cloud ensemble, including the processes of entrainment

155   of environmental air into the cloud, and detrainment of cloud condensate into the environment.

2.3 WCB identification

The ERA5-based WCB trajectories are calculated with a slightly modified version of the algorithm developed by Madonna et al. (2014). Based on the Lagrangian Analysis Tool (LAGRANTO; Wernli and Davies, 1997; Sprenger and Wernli, 2015), trajectories are started every 6 h from an equidistant grid in the lower troposphere and calculated forward for 48 h. For the

160   climatological analysis, the starting points are located every 80 km in the horizontal direction and vertically every 20 hPa

5

between 1050 and 790 hPa, consistent with Madonna et al. (2014). For the case study, the horizontal resolution of the starting grid is increased to 40 km. To be classified as WCB air parcels, the trajectories must experience a strong ascent of at least 600 hPa within 48 h in the vicinity of an extratropical cyclone, whereby extratropical cyclones are identified as two-dimensional objects based on the algorithm of Wernli and Schwierz (2006), refined in Sprenger et al. (2017). To exclude rapid ascent associated with tropical cyclones, the WCB trajectories are required to be north of 25°N during their ascent phase (at time 24 h). With respect to the WCB identification method by Madonna et al. (2014), two modifications are made: (i) Very fast ascending trajectories that fulfil the 600-hPa ascent criterion in the first part of the 48-h period and thereafter descend again are also selected. For those trajectories the pressure difference between times 0 and 48 h can be lower than 600 hPa and therefore they would have been neglected as WCB trajectories by the approach of Madonna et al. (2014). Compared to the original method, this leads to an increase in the number of identified WCB trajectories by about 35% (K. Heitmann, personal communication). (ii) WCB trajectories with a small distance to each other are clustered and considered to belong to the same WCB, with a clustering method similar to the one described in Catto et al. (2015). When one of the trajectories in the cluster is collocated with a surface cyclone for at least one time step during the ascent, all the trajectories in the cluster are considered as WCB trajectories. Compared to the original algorithm, where every single trajectory is required to be collocated with a surface cyclone, this leads to a further increase in the number of WCB trajectories by about 10%. Despite the significant increase in the number of identified WCB trajectories with respect to the original WCB identification criterion, tests have shown that the modifications do not affect the findings of this study.

In the present study, the WCB trajectories are classified according to their height into inflow (0-2 km height; corresponding to about 1000-800 hPa), ascent (2-7 km height and pressure $\sim$ 800-400 hPa) and outflow (>7 km height and pressure < 400 hPa), respectively.

2.4 Matches between WCB trajectories and CloudSat – CALIPSO overpasses

To combine the ERA5-based WCB trajectories with the satellite data, all WCB trajectories are selected that are overpassed by the CloudSat – CALIPSO satellites. Since the ~~satellite~~ individual satellite profiles along the tracks are available ~~at much higher temporal resolution~~ every about 0.16 s and therefore much more often than the hourly ERA5 data, the ERA5 fields are assumed to be representative for a 1-h time range of $\pm$ 30 minutes around each full hour. A match between a WCB trajectory position and the satellites' track occurs when the trajectory is located within 50 km horizontal distance of the satellite orbit during this 1-hour window ~~.~~ (see Fig. 2b). In total, ~~502'977~~ 509'042 matches are identified between individual WCB trajectories and A-Train overpasses in the nine winters. These matches are associated with about 9'000 different WCB clusters.

In the climatological study, several satellite profiles are attributed to each matching WCB trajectory. They are then averaged to increase the representativity of the observations (see schematic illustration in Fig. 1). In total, 113 satellite profiles are averaged per WCB match – that is, the profile with the closest distance to the WCB air parcel, plus the 56 preceding and the 56 succeeding profiles. ~~The average over~~ With a distance of 1.1 km between each satellite profile, the 113 assigned ~~satellite profiles corresponds~~ profiles correspond to a track segment length of about 124 km and therefore approximately the effective horizontal resolution of ERA5 (four times the horizontal grid spacing), i.e., the smallest scale the model is able to resolve fully

195 (see Abdalla et al., 2013). This allows for a better comparison between the observations and the model data. Consistent with earlier work (Illingworth et al., 2007; Delanoë et al., 2011), it is assumed that the narrow satellite track is representative for the three-dimensional model grid box.

2.5 Selection of strong WCBs

In addition to the analysis of the entire climatology of matching WCB trajectories, those with highest reflectivity values given
200 by CloudSat are investigated separately. More specifically, from all ~~502'977~~ 509'042 matches, in each 0.5 km height bin the 5% with highest reflectivities at their respective height are selected and referred to as "strong WCBs". These top 5% in terms of reflectivity are assumed to be the strongest cloud-and-precipitation producing WCB air parcels. Comparison of the entire climatology and the subcategory of "strong WCBs" allows to assess differences between the two categories in the cloud and precipitation structure, the geographical distribution, and the meteorological environment.

205 ## 3 Case study of a representative North Pacific WCB

In this Section we examine the cloud and precipitation structure of a representative WCB that occurred in January 2014 over the central North Pacific. The associated cyclone underwent an explosive deepening and was observed by the A-Train at the time of its strongest intensity (minimum sea level pressure of 975 hPa), around 00 UTC 3 January 2014. At this time the infrared satellite image and the overlaid ERA5 fields in Fig. 2a reveal a comma cloud pattern with high clouds along the cold, the
210 warm and the intense bent-back front, and a distinct dry slot that wraps around the storm centre below a cyclonically breaking upper-level wave, shown by the 2-pvu contour on 315 K. The yellow contour outlines the grid points where, according to the reanalysis data, at least one WCB air parcel is present somewhere in the vertical column. The large area encompassed by this contour indicates that the entire frontal region is influenced by WCB air. Note that these air parcels belong to WCB trajectories with a range of different starting times and vertical positions, with some still located at low levels at the beginning of their two-
215 day ascent, some in the middle of their ascent, and some already located in the upper troposphere at the end of their two-day ascent. As an example, Fig. 2b shows WCB trajectories with starting times at 06 UTC 2 January, and their position 18 h later (black dots), at the time of the satellite overpass.

The A-Train moved from the southeast to the northwest over the warm sector, the cold and the warm fronts of the mature cyclone (blue line in Fig. 2a,b), and thereby simultaneously captured parts of the WCB inflow, ascent and outflow. In the warm
220 sector, south of 27°N, the reflectivity profile measured by CloudSat (Fig. 3a,b) reveals shallow-to-midlevel convection above the WCB inflow, which is corroborated by the negative vertical gradient in equivalent potential temperature (θ_e) between the surface and 4 km height. Between 27° and 33°N the WCB inflow is cloud-free and located below thin cirrus clouds in the WCB outflow that increase in thickness toward the cold front. At the cold front, between 33° and 40°N, and above large parts of the surface warm front, between 42° and 46°N, most of the deep cloud system is associated with WCB air ~~, in particular~~
225 ~~at the cold front~~ (see purple dots in Fig. 3b that mark WCB air parcels). The high reflectivities (Fig. 3a) and satellite-retrieved IWC values (Fig. 3c) below 6-8 km indicate strong precipitation in the form of snow above and rain or melting snow below

the 0° isotherm. Unlike radars operating at centimetre wavelengths, which exhibit a clear reflectivity peak at the melting layer, CloudSat's millimetre operating wavelength does not lead to a typical bright band at the melting layer, but rather a dim band with reduced reflectivities (Sassen et al., 2007; Heymsfield et al., 2008). The dim band is due to snowfall attenuation and non-Rayleigh scattering effects, and it is evident both at the cold and at the warm front in the strongly precipitating cloud system (Fig. 3a). Above 6-8 km, at temperatures colder than about −20°C, the lower reflectivity and IWC values ~~indicate~~ suggest ice clouds rather than falling snow. At the cold front, in the unstable air south of 37°N the presence of some narrow columns with particularly high reflectivities suggest convective WCB ascent embedded in the frontal cloud. In the northern part of the cold front, the higher static stability and horizontally relatively uniform reflectivities point to a mainly stratiform cloud structure. At the warm frontal zone the WCB intersections with the satellite track indicate a gentle slantwise ascent along the tilted moist isentropes (Fig. 3b). North of 46°N the associated ice clouds decrease in thickness with increasing distance from the surface warm front, as the cloud base slopes upward along the moist isentropes and the cloud-top height decreases.

Figure 3d shows in colours the sum of the prognostic cloud ice and snow variables of ERA5, interpolated along the satellite track. To allow for a better comparison with the observations, in Fig. 3e the satellite-retrieved IWC is shown as the running mean over 113 satellite profiles, which corresponds to a track length of 124 km and thereby approximately the effective resolution of ERA5 (i.e., four times the horizontal grid spacing, see Abdalla et al., 2013). As noted in Sect. 2.1, the observations and ERA5 are not entirely independent, as the satellite-retrieved IWC relies on thermodynamic variables from ECMWF analyses. In particular, the retrieved IWC is based on temperature profiles from the ECMWF to locate the melting layer height, which implies that by design the melting layer agrees well with ERA5. Despite this constraint, the satellite retrievals contain much additional information that is independent from the ECMWF data, such that the comparison with ERA5 is meaningful and provides important insight into the quality of the model data.

Comparison of Fig. 3d and e shows that ERA5 captures the location of the cloud system and the broad ice and snow structure remarkably well. The ~~values strongly increase~~ sum over the ice and snow values strongly increases toward the melting layer and ~~peak~~ peaks right above the melting layer in the deep frontal clouds, where most of ~~the frozen fraction~~ it is present as falling snow (see ~~grey contours~~ thin black contours in Fig. 3d). However, the model considerably underestimates the peak values between the melting layer and the −20°C isotherm (maxima of $1050\,\mathrm{mg\,m^{-3}}$ in ERA5 compared to $1630\,\mathrm{mg\,m^{-3}}$ in the observations), which are most likely associated with mixed-phase clouds. The underestimation is particularly pronounced in the convective clouds south of 27°N. The one standard deviation percentage errors associated with the IWC retrievals in this case study are about 20-30% in the thin ice clouds at upper levels, 5-20% around the −20°C isotherm and 10-40% near the melting layer (not shown). The differences between the observations and ERA5 near the melting layer are therefore outside the error range of the observations, even for values of 40%. Furthermore, along the entire cross section the cloud edges are less sharp in ERA5 than in the observations, and the transition between cloudy and cloud-free regions is smoother. Nevertheless, comparison with ERA5's predecessor, ERA-Interim, reveals a strong improvement in the ice cloud representation in ERA5 (Binder, 2016). In ERA-Interim, the agreement with the observed IWC is very poor, in particular in the mixed-phase clouds, where the underestimation of the high values close to the melting layer amounts to several orders of magnitude. The significant improvement of the representation from ERA-Interim to ERA5 can mainly be explained by a major upgrade of the cloud and

precipitation parameterisation (see also Delanoë et al., 2011; Forbes and Ahlgrimm, 2014): While ERA5 is based on prognostic variables for cloud ice, snow, liquid water and rain, in ERA-Interim precipitation and mixed-phase clouds are described by diagnostic formulations, and snow is not present in the ~~IWC variable~~ frozen hydrometeor fraction but directly removed from the atmospheric column.

In summary, the case study of this North Pacific WCB reveals that (i) WCB air parcels form part of vertically extended, strongly precipitating clouds, but not the entire frontal cloud system is WCB air, (ii) convection can occur in the WCB inflow and ascent region, consistent with previous studies (e.g., Crespo and Posselt, 2016; Oertel et al., 2019), and (iii) the ERA5 reanalysis with prognostic variables for snow and ice is able to capture the broad structure and distribution of the frozen hydrometeor fraction associated with the WCB cloud, but the peak values are underestimated.

4 Climatological analysis of the WCB cloud structure

In this Section the WCB clouds and their meteorological environment will be characterised climatologically for nine Northern Hemisphere winters. We will first discuss the spatial distribution of the matches between WCB trajectories and the A-Train, and then investigate their vertical structure in satellite observations and reanalysis fields.

4.1 Spatial distribution of the intersected WCB trajectories

Figure 4a shows the spatial distribution of the ~~502'977~~ 509'042 matches between individual WCB trajectories and the A-Train overpasses. Matches occurred almost in the entire extratropics, but the highest number is present over the North Pacific and North Atlantic storm track regions between about 30° and 60°. This spatial pattern reflects the winter climatological distribution of WCBs during their inflow, ascent and outflow (blue contours). In general, in the southwestern ocean basins most WCB air parcels were observed in the inflow, i.e., when the WCB trajectories were below 2 km height (pressure levels > 800 hPa), in agreement with the climatological maximum of WCB starting positions (Madonna et al., 2014). In contrast, in the northeastern part of the oceans, at the end of the storm tracks, the majority of the matches occurred in the outflow, i.e., when WCB trajectories were above 7 km height (pressure levels < 400 hPa). Overall, the matches are distributed over a wide altitude range between the surface and 13 km height, with the highest numbers below 2 km in the inflow and in particular between 7 and 10 km in the midlatitude outflow (Fig. 4c). The latitude of the matches increases from about 25°-50°N in the WCB inflow to 35°-75°N for air parcels at 8 km height (mean and 10-90 interpercentile range in ~~black~~ green in Fig. 4d), reflecting the poleward motion typically occurring during the WCB ascent. Note, however, that the WCB air parcels in the different height bins generally belong to different WCB trajectories – only in rare cases the same trajectory has been observed more than once by the narrow CloudSat–CALIPSO tracks. Matches above 8 km typically occurred again at lower latitudes (where the tropopause is higher than in polar region), ranging from about 30° to 60°N for air parcels at 10 km height, and from 10° to 35°N for very high outflow above 12 km. These matches are most likely associated with WCBs in convectively active subtropical systems.

The matches with "strong WCBs", that is, the 5% of the air parcels in each 0.5 km height bin with the highest CloudSat radar reflectivities (see Section 2.5), are mainly located over the North Pacific and North Atlantic (Fig. 4b). Interestingly, in the inflow and early ascent (< 3.5 km) the mean latitude of the WCB air parcels with exceptionally strong reflectivities is further north than the mean over all trajectories, with most air parcels located between $30°$ and $60°$N (mean and 10-90 interpercentile range in ~~red~~ blue in Fig. 4d). The opposite is true at higher altitudes, where the strong WCBs are typically located much further south than the entire climatology. Between 4 and 10 km height their mean latitude is approximately constant around $38°$N, and matches at higher levels occur again at very low latitudes and are probably related to subtropical cyclones. Note, again, that different WCBs contribute to the strong category in each height bin, and the general decrease in the mean latitude from inflow to outflow observed for the strong WCBs does not imply an equatorward ascent. All in all, the analysis shows that WCBs with exceptionally strong radar reflectivities in their inflow occur further north than the mean of all matches, while higher than usual radar reflectivities in the WCB ascent and outflow are found further south.

4.2 Composites of reflectivity and DARDAR-retrieved IWC

To investigate the cloud structure of the WCBs during their inflow, ascent and outflow, we create vertical composites of the satellite observations, separately for different WCB heights. Hereby, all matching WCB air parcels are classified into 0.5 km height bins, with the number of matches per bin shown in the histogram in Fig. 4c. We will first examine the composites associated with the entire climatology, and then compare them to the subcategory of strong WCBs.

4.2.1 All WCBs

Figure 5 shows composites of vertical profiles of CloudSat reflectivity (Fig. 5a) and DARDAR-retrieved IWC (Fig. 5b) as a function of the height at which the A-Train profile matched with a WCB trajectory. This height is referred to as z_{WCB}. For instance, for matches at a height of $z_{WCB} = 3$ km, the radar reflectivity shows median values [1] exceeding -6 dBZ from near the ground to about 6 km altitude, whereas for matches above $z_{WCB} = 7$ km, radar reflectivities are below -30 dBZ, if the median is calculated over all WCBs (Fig. 5a). Thus, with increasing z_{WCB} the composites give insight into the vertical cloud structure associated with the WCB inflow ($z_{WCB} = 0$-2 km), ascent ($z_{WCB} = 2$-7 km) and outflow ($z_{WCB} > 7$ km), respectively. Comparison with the latitude-height distribution of the matches (~~thick black~~ green line in Fig. 4d) shows that up to $z_{WCB} \approx 8$ km the satellite composites can be interpreted as a – somewhat irregular – vertical cross section from south to north through poleward ascending WCB air. However, keep in mind that the matching WCB air parcels in the different height bins correspond to different WCB trajectories, such that Fig. 5 shows a composition of single WCB positions and not the development along individual trajectories. <u>The calculation of median rather than mean profiles of the matches is motivated by the fact that in the case of reflectivity the median allows us to take into account clear-sky values, and in the case of IWC the mean would be dominated by large values.</u> As seen in the case study, several matches can occur on top of each other in the same cloud system (see purple dots in Fig. 3b). In these cases, in the composites the same satellite profile is taken into account for

---

[1] ~~For the reflectivity and IWC fields it is more meaningful to show the median value rather than the mean. In the case of reflectivity this allows us to take into account clear-sky values, and in the case of IWC the mean would be dominated by large values.~~

each match separately, i.e., it is present more than once along the x-axis. In summary, this sophisticated compositing approach is
325 able to provide representative vertical profiles of observed radar reflectivity and IWC along WCBs in the Northern Hemisphere storm track regions in winter.

To quantify how often WCB matches occur on top of each other in the same cloud system, the contours in Fig. 5a,b show the relative WCB trajectory frequency, which is the number of matches in a certain $0.5\,\mathrm{km}$ profile height bin normalised by the total number of matches in the specific WCB height bin. For instance, a relative frequency of ~~25~~10% at $z_{WCB} = 3.75\,\mathrm{km}$
330 and a profile height ~~$z_{prof} = 8.75$~~$z_{prof} = 9.75\,\mathrm{km}$ indicates that ~~25~~10% of the WCB trajectories located between 3.5 and 4 km height have another WCB trajectory on top of them between ~~8.5 and 9~~9.5 and 10 km height. Such a situation occurred, for instance, in the case study between about $36°$ and $45°$N in the deep cold and warm frontal clouds (Fig. 3b). For matches at $z_{WCB} = 1\,\mathrm{km}$ height, only in ~~10~~5% of the cases another WCB trajectory is located on top of them at ~~8.5-9~~9.5-10 km height. The vertical area in between can either also be associated with WCBs (as in the case study between $36°$ and $42°$N; Fig. 3b)
335 or not (as between $30°$ and $36°$N in Fig. 3b) – the frequency values do not provide insight into the vertical connectivity of the WCB air. By definition, the frequency is 100% along the diagonal line, and the slower its decrease away from the diagonal the more the observed reflectivity and IWC patterns are associated with WCB air.

In the reflectivity composite, the white areas indicate either clear air, or, in particular below about $0.8\,\mathrm{km}$ height, ground clutter, which both have been filtered out (see Section 2.1). In the IWC composite, the white areas indicate the absence of
340 frozen hydrometeors. The cloud-top heights according to the radar reflectivities are everywhere lower than those according to the IWC retrievals. This can be explained by the inability of the radar to detect thin ice clouds with reflectivities below $-30\,\mathrm{dBZ}$, whereas for the IWC retrievals the radar measurements are combined with lidar data that is strongly sensitive to optically thin ice clouds (see Section 2.1).

Overlaid on top of the observed fields are ERA5-based temperature contours (red dashed lines in Fig. 5a,b) and the dynam-
345 ical tropopause (brown ~~2 pvu~~ 2-pvu contour in Fig. 5a,b). From $z_{WCB} = 0\,\mathrm{km}$ up to about $z_{WCB} = 8\,\mathrm{km}$~~(thick black line in Fig. 4d)~~, the melting layer and the dynamical tropopause decrease in height (Fig. 5a,b), consistent with the increase in mean latitude (~~thick black~~ green line in Fig. 4d), while between $z_{WCB} = 8$ and 14 km the transition from predominantly subpolar to subtropical outflow is associated with an increase in their heights. At the height of the WCB inflow (z_{WCB} and $z_{prof} \approx 0$-2 km), liquid clouds with reflectivities of about -10 to $-5\,\mathrm{dBZ}$ are present above the ground clutter (Fig. 5a), indicating some
350 drizzle or light rain (Stephens and Haynes, 2007). Above the inflow, the small non-zero median IWC values reveal the presence of thin ice clouds that extend up to about ~~9~~9-10 km height (Fig. 5b). As suggested by the low reflectivities below $-30\,\mathrm{dBZ}$, this is most likely non-precipitating cirrus. The ~~10~~5% WCB trajectory contour approximately follows these ice clouds, indicating that a small fraction of them is associated with WCB air.

During the ascent ($z_{WCB} \approx 2$-7 km) WCBs form part of deep clouds, with cloud-top heights just below the ERA5-based
355 dynamical tropopause at 9-10 km (Fig. 5a,b). The clouds have relatively high reflectivity values up to $> 4\,\mathrm{dBZ}$ and – between the melting layer and about $-20°$C – high DARDAR-retrieved IWC with peaks at $260\,\mathrm{mg\,m^{-3}}$, which indicates precipitation in the form of snow above and rain below the melting layer. The highest IWC values occur approximately at the height of the WCB, whereas the highest reflectivities are present just below the WCB ~~near~~ slightly above the melting layer. The peak

values, and therefore most likely the strongest surface precipitation, occur when the WCB trajectories are at a height of about $z_{WCB} = 3.5\text{-}4$ km. Compared to the inflow, the WCB trajectory densities above and below the diagonal are higher in most of the ascent region, indicating a stronger contribution of WCB air to the reflectivity and IWC profiles. Of course, there is a large case-to-case variability, and the median profiles contain cloud systems that are almost entirely formed by strongly ascending WCB air, and others where only a small part of the deep cloud is WCB air. The decrease in the WCB densities to only ~~10-25~~about 10% at cloud base and cloud top suggests that the latter is often the case, i.e., the WCB ascent is typically embedded in a deeper cloud that forms partially due to air parcels with a weaker ascent than required for the WCB criterion.

In contrast to the ascent, the WCB outflow ($z_{WCB} > 7$ km) is located within an about 3 km deep cirrus layer with low reflectivities below the sensitivity of the radar (Fig. 5a) and low IWC (1-10 mg m^{-3}, Fig. 5b). Their cloud bases and tops increase gradually with increasing outflow height, which suggests a predominantly slantwise ascent along the baroclinic zone, similar to the pattern observed in the case study north of 46°N (Fig. 3). The deep cirrus layer and the extension of ice clouds above the WCB outflow level are in line with the findings of Wernli et al. (2016), who showed that the WCB outflow is often associated with cirrus clouds that form by freezing of liquid droplets during the strong ascent, while above the outflow in situ ice cloud formation can occur in response to the strong lifting associated with the WCB.

4.2.2 Strong WCBs

Analogous to the satellite composites created for all WCB matches, Fig. 5c,d shows the median reflectivity and IWC profiles for the subcategory of strong WCBs, together with ERA5-based temperature contours and the dynamical tropopause. The slight decrease in latitude with increasing height of the WCB matches (~~red~~ blue line in Fig. 4d) is reflected in a general increase in the melting layer height and the tropopause along the x-axis (Fig. 5c,d), in contrast to the decrease observed for the entire climatology (Fig. 5a,b). It is again important to keep in mind that these composites cannot be interpreted in a Lagrangian way; the WCB air parcels in the different height bins generally belong to different WCB trajectories and the overall decrease in latitude with increasing z_{WCB} does not imply an equatorward ascent.

At the height of the WCB (along the diagonal), but also above and below, the reflectivities exceed those of all matches by 10-25 dBZ. Above the melting layer this goes along with DARDAR-retrieved IWC values that are a factor of 5-5000 larger than those of all matches (Fig. 5d). This confirms that the top 5% of the matches in terms of radar signal are indeed very strongly cloud-and-precipitation-producing WCB ~~air~~ trajectories. Deep clouds extending from the surface to the tropopause occur not only in the ascent region, but – in contrast to all matches – also above the inflow and in the outflow. The cloud-top height according to the IWC pattern is at 10 km above the air parcels in the WCB inflow, at 11 km for the ascending ones and at 11-14 km for the outflow, and it is thus everywhere higher than for the entire climatology. The decrease in the WCB trajectory densities away from the diagonal is much slower than for all matches, implying a stronger contribution of WCB trajectories to the formation of the deep clouds. Presumably, WCB trajectories in the inflow, ascent and outflow are often located on top of each other in the same cloud system, as ~~seen~~ in the case study at the cold front (Fig. 3b). These results also indicate that a vertically deep layer of trajectories fulfilling the WCB criterion is likely leading to particularly high reflectivities and intense surface precipitation. The peak reflectivities (13.9 dBZ compared to ~~4.4~~4.2 dBZ for all matches) occur at the height of the

ascending WCB and not below as for all matches, and ~~there is no clear indication for a melting layer in the radar signal~~ the signal decrease below the WCB indicates strong snow and rain attenuation. The IWC maxima (~~1190~~1180 mg m^{-3} compared to 260 mg m^{-3} for all matches) are collocated with the reflectivity maxima. They extend over several WCB heights along the diagonal, from about $z_{WCB} = 2.5$ km to $z_{WCB} = 5$ km, in contrast to the rather localised peak at $z_{WCB} = 3.5\text{-}4$ km observed for all matches. A secondary reflectivity and IWC maximum occurs at $z_{WCB} > 12$ km in the middle troposphere, below the WCB outflow, and the low latitude of these matches (Fig. 4d) suggests that it is most likely associated with subtropical cyclones.

4.3 Meteorological environment in ERA5

To analyse the WCB clouds and the differences between all and strong WCBs in more detail, we complement the satellite observations with model data from ERA5. This allows us to gain insight into the meteorological environment associated with the matches, and, at the same time, to compare the modelled ice and snow water content with the DARDAR observations. To this end, vertical profiles of the ERA5 fields are interpolated to the position of the matches, and composites equivalent to those discussed in the previous Section are created. Again, we will first examine the fields for all WCB matches and then compare them with the subcategory of strong WCBs.

4.3.1 All WCBs

The vertical composites of various ERA5 fields are shown in Fig. 6, separately for different WCB heights. [1] Except for the frozen and liquid hydrometeor content the mean rather than the median profiles are shown in each height bin, as the fields are slightly smoother, but the median profiles are very similar. The frozen hydrometeor fraction, i.e., the sum of the prognostic cloud ice and snow variables (Fig. 6a), resembles the observed pattern in Fig. 5b remarkably well. However, in the ascent region between the melting layer and about $-20°$C the peak values are underestimated (160 mg m^{-3} in ERA5 vs. 260 mg m^{-3} in the observations), whereas above the inflow and below the outflow the values are overestimated, and the cirrus layer associated with the outflow is considerably deeper than in the observations. Also the transition between cloudy and cloud-free regions is smoother. ~~The~~ Since the composites consist of a large number of satellite profiles, the mean errors associated with the IWC retrievals are much lower than the single values in the case study, with maximum errors of 0.17% coinciding with the maximum observed IWC values (not shown). The difference between the IWC values in ERA5 and the observations are therefore much larger than the observational uncertainty range, both for the underestimated values in the ascent region and the overestimated values above the inflow and below the outflow. The underestimation of the peak values close to the melting layer is consistent with the case study. It occurs in a 2-3 km deep layer with mixed-phase clouds (Fig. 6b), which are known to be difficult to simulate and associated with large uncertainties in many numerical weather prediction and climate models (e.g., Morrison et al., 2003; Illingworth et al., 2007; Klein et al., 2009; Delanoë et al., 2011).

---

[1] ~~Except for the frozen and liquid hydrometeor content the mean rather than the median profiles are shown in each height bin, as the fields are slightly smoother, but the median profiles are very similar.~~

The ice clouds in ERA5 coincide with high relative humidities with respect to ice (RH_{ice}; Fig. 6c). The values are close to saturation ($> 80\%$) along most of the WCB on the diagonal, and they are particularly high in a deep layer in the ascent region, where the strong updraft continuously leads to new ice cloud formation. At lower altitudes, the inflow and especially the ascent regions are also associated with high cloud liquid water and rain water contents (Fig. 6b). The liquid hydrometeor fraction extends from the surface up to about 5-6 km height, with a 2-3 km deep layer of supercooled liquid water co-existing with ice above the melting layer. The highest liquid hydrometeor values occur during the WCB ascent (z_{WCB} at $\approx$ 2-4 km) slightly below the WCB and the melting layer, in the lower part of the vertically extended cloud. Accordingly, also the surface precipitation has a maximum when the WCB is at 2-4 km height, with values of about $1.8\,\mathrm{mm\,h^{-1}}$ (solid green line in Fig. 7). Surface precipitation is also high in the WCB inflow ($1.2\text{-}1.5\,\mathrm{mm\,h^{-1}}$), whereas it is rather weak below the outflow ($0.3\,\mathrm{mm\,h^{-1}}$). For $z_{WCB} > 6 - 7\,\mathrm{km}$, the frozen and liquid hydrometeors are vertically disconnected (Fig. 6a,b), consistent with the tongue of relatively low $RH_{ice} < 70\%$ in between (Fig. 6c). This suggests that the weak surface precipitation evident for $z_{WCB} > 6 - 7\,\mathrm{km}$ (Fig. 7) is not associated with the WCB, but with the low-level warm clouds present at 1-2 km height below the WCB (Fig. 6b). Throughout the inflow, ascent and outflow, most of the surface precipitation is associated with the large-scale cloud scheme (Fig. 7). Convective precipitation is significantly lower, but has a small peak in the inflow and early ascent. The presence of convection in the inflow is further corroborated by very low moist static stability values (i.e., weak vertical gradients in equivalent potential temperature, $d\theta_e/dz$) in that region (Fig. 6d,e). Higher stabilities are present below the ascending WCB, where the tilted moist isentropes indicate a lifting over the cold or warm front (Fig. 6d). At higher altitudes during the ascent, at and above the height of the WCB, the stabilities are again lower and indicate some convective motion.

The strong cloud and precipitation formation goes along with elevated PV values in the lower and middle troposphere, and low PV in the WCB outflow (Fig. 6f). The elevated ~~low~~ low- and mid-level PV ($> 0.5\,\mathrm{pvu}$) extends over a broad and deep region in the inflow, ascent and early outflow (z_{WCB} at $\approx$ 1-10 km) ~~,~~ and coincides with increased stability (Fig. 6e). Two areas with particularly high PV ($> 0.7\,\mathrm{pvu}$) are located slightly below the ascending WCB (z_{WCB} at $\approx$ 2-5 km; Fig. 6f). One of these two high low-level PV areas is located between the melting layer and the observed and modelled snow and ice maximum at WCB height (Figs. 5b and 6a), and it coincides with the radar reflectivity maximum (Fig. 5a). Most likely, latent cooling of the melting layer, as well as latent heating due to freezing of cloud water and vapour deposition on ice particles along the WCB, both contribute to the PV maximum in between. The agreement with the observations indicates that in addition to the good representation of cloud ice and snow in ERA5, the reanalysis data is able to capture the cloud-diabatic processes associated with WCBs and their impact on the dynamics very well. The second area with high low-level PV (at $z_{WCB} \approx$ 2-3 km) is located below the melting layer at 1-2 km profile height and coincides with the maximum in the modelled cloud rain and liquid water content (Fig. 56b), which suggests that here the PV production is mainly associated with latent heating due to condensation, and potentially some below-cloud cooling due to rain evaporation. This PV maximum is not accompanied by a corresponding maximum in reflectivity (Fig. 5a), probably as a result of the two-way attenuation of the radar signal close to the surface in strongly precipitating systems. In the WCB outflow, the PV values are anomalously low ($< 0.2\,\mathrm{pvu}$; Fig. 6f) and coincide with reduced vertical stability (Fig. 6e). As a consequence of the low-PV air in the outflow, the tropopause above is elevated, and a sharp vertical PV gradient is established between the low values at WCB height and the high values in the stratosphere. The

elevated tropopause also goes along with an increased vertical gradient in equivalent potential temperature and a layer with peak vertical stability in the stratospheric air above the WCB outflow (Fig. 6d,e), which is referred to as tropopause inversion layer (TIL; Birner et al., 2002). As discussed by Kunkel et al. (2016), the TIL typically forms above the WCB, because (i) the low-level cloud-diabatic processes lead to an increase in the vertical motion and an enhancement of static stability above the updraft region, and (ii) the upward transport of moisture into the tropopause region and the formation of high-level ice clouds goes along with strong radiative cooling at the tropopause, which contributes to a further enhancement of the TIL.

4.3.2 Strong WCBs

The vertical composites of the ERA5 fields for the subcategory of strong WCBs are shown in Fig. 8. Again, the reanalysis correctly captures the broad structure and distribution of ice and snow along the WCBs (compare Fig. 8a and Fig. 5d), but underestimates the peak values in the mixed-phase layer (~~490~~540 mg m^{-3} in ERA5 vs. ~~1190~~1180 mg m^{-3} in the observations). The observational uncertainty of the IWC values is slightly larger than for the entire climatology, with maximum values of about 1% in the ascent region near the melting layer (not shown), but the difference between the observed and ERA5-based IWC maxima is still significantly larger than the uncertainty range of the observations. Consistent with the satellite measurements (Fig. 5c,d), throughout the inflow, ascent and outflow the modelled clouds associated with the strong WCBs are considerably deeper than those associated with the entire climatology, their hydrometeor contents are higher, the layer with mixed-phase clouds is deeper (Fig. 8a,b), and RH$_{ice}$ is higher (Fig. 8c). This goes along with considerably higher surface precipitation along the entire WCB, with peak values above 3 mm h^{-1} when the air parcels are at 3.5 km height, and significant amounts also in the inflow and below the outflow (solid blue line in Fig. 7). In contrast to all WCB matches, ~~up to $z_{WCB} \approx 9$ km~~ there is no gap between the frozen and liquid hydrometeors throughout the inflow, ascent and outflow (Fig. 8a,b), consistent with the higher RH$_{ice}$ (Fig. 8c). This suggests that also above $z_{WCB} \approx 6$ km the surface precipitation is coming from the WCB, and not from the low-level warm clouds as in the case of all matches. Along the entire WCB, most of the precipitation is again associated with the large-scale cloud scheme. The strongest convective precipitation occurs for WCBs around 4-5 km height and is potentially linked to a local minimum in moist static stability in the lower troposphere in that region (Fig. 8d,e). High values in the convective precipitation are also present at $z_{WCB} > 12$ km, where high reflectivities and IWC values have been observed below the WCB outflow in Fig. 5c,d. The presence of convection in this region is further supported by the high θ_e values (Fig. 8d), the weak stratification (Fig. 8e) and the high RH$_{ice}$ (Fig. 8c) throughout the depth of the troposphere. As mentioned in Section 4.2.2, this secondary cloud and precipitation maximum is most likely linked to subtropical cyclones.

The stronger cloud and precipitation formation in the subcategory of strong WCBs is reflected in stronger low-level PV production, in particular for WCBs in the inflow and early ascent, with peak values > 0.9 pvu (Fig. 8f). In contrast to the entire climatology, where the highest PV values are located just below the WCB, for the strong category they occur along the WCB on the diagonal and coincide with the observed reflectivity and ice and snow maxima (Fig. 5c,d). Along the WCB, we expect the strongest latent heating due to condensation, freezing and vapour deposition on ice, consistent with the relative humidity maximum (Fig. 8c). Thus, the positive PV maximum coincides with the latent heating maximum, which is in line with the findings from previous studies (e.g., Wernli and Davies, 1997). In the WCB outflow, the PV values are anomalously low ~~PV~~

($< 0.2\,\mathrm{pvu}$). As for the entire climatology, above the outflow the tropopause is elevated and a tropopause inversion layer is evident (Fig. 8e,f).

5   Summary and discussion

495   In this study, ERA5 reanalyses have been combined with satellite observations from the polar-orbiting CloudSat radar and CALIPSO lidar to gain a detailed observational perspective on the vertical cloud structure of WCBs during their inflow, ascent and outflow, and to evaluate their representation in ERA5. To this end, more than 500'000 matches between the satellite observations and ERA5-based WCB trajectories (corresponding to about 9'000 different WCB clusters) were evaluated during nine Northern Hemisphere winters in a composite analysis and a detailed case study. The majority of the matches occurred 500   over the ocean basins in regions of high climatological WCB frequencies and can therefore be considered as representative.

The satellite observations revealed that the WCBs form part of vertically extended, strongly precipitating clouds, in particular during their ascent, with cloud-top heights at 9-10 km. In some cases the entire cloud system is associated with WCB air, but often the cloud parts below and above the WCB air parcels form in air with a comparatively weak ascent below the WCB threshold. Convection can occur above the WCB inflow and during the ascent, in agreement with recent studies on convection 505   embedded in WCBs (e.g., Crespo and Posselt, 2016; Flaounas et al., 2016; Oertel et al., 2019). In the upper troposphere, after the main ascent phase, the WCBs are typically located near the top of an about 3 km deep layer with cirrus clouds.

According to ERA5, high low-level PV occurs below the ascending WCB in the lower part of the vertically extended cloud. The strongest low-level PV production occurs at about 3 km height between the melting layer and the ascending WCB and coincides with the radar reflectivity maximum. It is most likely produced by a combination of diabatic heating due to 510   freezing of cloud water and depositional growth of ice particles at the WCB height and diabatic cooling from snow melting below. A second area with particularly strong low-level PV production occurs at about 1-2 km height, below the WCB and the melting layer, in a region with strong cloud-condensational heating, and possibly some below-cloud evaporative cooling. The occurrence of the strongest positive PV anomalies below rather than at the WCB height is surprising, and the potentially important contribution of various in- and below-cloud microphysical processes to the low-level PV production is in line with 515   the findings from recent modelling studies (Joos and Wernli, 2012; Crezee et al., 2017; Attinger et al., 2019).

The WCB trajectories with the highest reflectivity values ("strong WCBs") have mainly been observed over the North Atlantic and North Pacific, and – except in the inflow – at relatively low latitudes ($\sim 38°\mathrm{N}$). They are associated with particularly deep and strongly precipitating clouds that occur not only during the ascent, but also in the inflow and outflow region. Compared to the climatology of all WCBs, the hydrometeor content is considerably higher and the surface precipitation is stronger. 520   The low-level PV production is larger and has its peak in the inflow and early ascent at the height of the WCB, and it coincides with high reflectivities and hydrometeor values. The agreement of the positive PV anomaly with the region of strong cloud formation is characteristic for strongly ascending WCB air masses, where the PV anomaly, which is produced below the diabatic heating maximum, is advected upward toward the heating maximum (Wernli and Davies, 1997).

16

The comparison between the satellite retrievals and ERA5 showed that the reanalyses are able to capture the main structure of the WCB clouds in terms of position and thermodynamic cloud phase. The spatial pattern of the frozen hydrometeor fraction (ice and snow) is in good agreement with the observations, in particular at high altitudes, where most of the frozen fraction is present as ice rather than falling snow. However, the peak values in the mixed-phase cloud regime near the melting layer are underestimated by a factor of 1.6 for the entire climatology and a factor of 2.4 for the subcategory of strong WCBs. This corroborates the findings from many other studies that mixed-phase clouds are difficult to simulate accurately (e.g., Illingworth et al., 2007; Delanoë et al., 2011). The co-existence of ice, supercooled liquid water and water vapour, and the complex interaction of various microphysical processes, render their understanding and parameterization in numerical weather prediction and climate models particularly challenging. Nevertheless, compared to the older reanalysis dataset ERA-Interim (Dee et al., 2011), where the microphysical parameterisations are based on simplified diagnostic relationships for snow and mixed-phase clouds, the improved scheme in ERA5 with prognostic variables for cloud ice, snow, liquid water and rain leads to a much more realistic representation of the WCB cloud pattern (Binder, 2016). This is consistent with the findings from Delanoë et al. (2011) and Forbes and Ahlgrimm (2014), who also compared CloudSat–CALIPSO observations with two ECMWF models with schemes similar to the ones in ERA5 and ERA-Interim, respectively, and found a significant improvement in the ice-cloud parameterization with the upgrade from the diagnostic to the prognostic representation of mixed-phase clouds and precipitation. As a caveat of the present study, it should be noted that the DARDAR-retrieved IWC depends on thermodynamic variables like temperature, pressure and specific humidity from ECMWF analyses and is therefore not entirely independent of the ERA5 data being evaluated. This illustrates the challenge of finding completely independent observations to validate cloud variables in model data. Nevertheless, the satellite retrievals contain much additional information not incorporated in ERA5 and thereby they allow for a meaningful comparison of the two data sets.

Following earlier studies (e.g., Illingworth et al., 2007; Delanoë et al., 2011), in the present analysis it has been assumed that the cloud structure observed along the narrow two-dimensional satellite track is representative for the entire three-dimensional volume of the model grid box. Despite a quite good agreement between ERA5 and the observations, it is possible that this assumption is not entirely justified and the clouds observed by the satellite are not representative for the larger-scale features. As proposed by Delanoë et al. (2011), additional information on the large-scale environment could be obtained from other instruments onboard the A-Train satellites with a wider swath width, in order to better assess the representativity of the measurements.

The CloudSat and CALIPSO measurements have provided a much needed, detailed observational perspective into the internal cloud structure of WCBs, and have revealed many small- and mesoscale structures not resolved by the temporally and spatially much coarser-resolution model data that has mainly been used so far to study WCBs. The measurements complement the insight gained on WCBs from recent modelling studies with high-resolution convection-permitting simulations (e.g., Oertel et al., 2020). In future work, the large number of WCB trajectories observed by CloudSat and CALIPSO could still be exploited in more detail, both in case studies and climatological analyses. They could be classified, for instance, according to different criteria like the position relative to the cyclone centre and the stage of the cyclone life cycle, the ascent behaviour (slantwise vs. convective), the outflow curvature (cyclonically vs. anticyclonically), the amplitude of the low-level positive

and upper-level negative PV anomalies or the geographical region, in order to assess whether different types of WCBs have
560 common characteristics. It would also be insightful to extend the climatological analysis to different seasons and the Southern Hemisphere, to investigate potential seasonal and hemispheric differences in the WCB cloud structure. Finally, the study could be repeated with data from other models. In particular, it would be interesting to evaluate the representation of WCBs in operational numerical weather prediction models at different lead times, which might allow for the identification of systematic forecast errors.

References

Abdalla, S., Isaksen, L., Janssen, P., and Wedi, N.: Effective spectral resolution of ECMWF atmospheric forecast models, ECMWF Newsletter, 137, 19–22, 2013.

Attinger, R., Spreitzer, E., Boettcher, M., Forbes, R., Wernli, H., and Joos, H.: Quantifying the role of individual diabatic processes for the formation of PV anomalies in a North Pacific cyclone, Quart. J. Roy. Meteor. Soc., 145, 2454–2476, 2019.

Bechtold, P., Semane, N., Lopez, P., Chaboureau, J.-P., Beljaars, A., and Bormann, N.: Representing equilibrium and nonequilibrium convection in large-scale models, J. Atmos. Sci., 71, 734–753, 2014.

Binder, H.: Warm conveyor belts: cloud structure and role for cyclone dynamics and extreme events, Ph.D. thesis, ETH Zürich, Nr. 24016, https://doi.org/10.3929/ethz-b-000164982, 2016.

Binder, H., Boettcher, M., Joos, H., and Wernli, H.: The role of warm conveyor belts for the intensification of extratropical cyclones in Northern Hemisphere winter, J. Atmos. Sci., 73, 3997–4020, 2016.

Birner, T., Dörnbrack, A., and Schumann, U.: How sharp is the tropopause at midlatitudes?, Geophys. Res. Lett., 29, 45–1, 2002.

Bjerknes, J. and Solberg, H.: Life cycle of cyclones and the polar front theory of atmospheric circulation, Geophys. Publ., 3, 1–18, 1922.

Blanchard, N., Pantillon, F., Chaboureau, J.-P., and Delanoë, J.: Organization of convective ascents in a warm conveyor belt, Weather Clim. Dynam. Discuss., 2020, 1–32, https://doi.org/10.5194/wcd-2020-25, 2020.

Browning, K. A.: Organization of clouds and precipitation in extratropical cyclones, in: Extratropical Cyclones: The Erik Palmén Memorial Volume, edited by Newton, C. W. and Holopainen, E. O., pp. 129–153, Amer. Meteor. Soc., 1990.

Carlson, T. N.: Airflow through midlatitude cyclones and the comma cloud pattern, Mon. Wea. Rev., 108, 1498–1509, 1980.

Catto, J. L., Madonna, E., Joos, H., Rudeva, I., and Simmonds, I.: Global relationship between fronts and warm conveyor belts and the impact on extreme precipitation, Journal of Climate, 28, 8411–8429, 2015.

Crespo, J. A. and Posselt, D. J.: A-Train-based case study of stratiform-convective transition within a warm conveyor belt, Mon. Wea. Rev., 144, 2069–2084, 2016.

Crezee, B., Joos, H., and Wernli, H.: The microphysical building blocks of low-level potential vorticity anomalies in an idealized extratropical cyclone, J. Atmos. Sci., 74, 1403–1416, 2017.

Davis, C. A. and Emanuel, K. A.: Potential vorticity diagnostics of cyclogenesis, Mon. Wea. Rev., 119, 1929–1953, 1991.

Dee, D. P., Uppala, S. M., Simmons, A. J., Berrisford, P., Poli, P., Kobayashi, S., Andrae, U., Balmaseda, M. A., Balsamo, G., Bauer, P., et al.: The ERA-Interim reanalysis: Configuration and performance of the data assimilation system, Quart. J. Roy. Meteor. Soc., 137, 553–597, 2011.

Delanoë, J. and Hogan, R. J.: A variational scheme for retrieving ice cloud properties from combined radar, lidar, and infrared radiometer, J. Geophys. Res., 113, D07 204, https://doi.org/10.1029/2007JD009000, 2008.

Delanoë, J. and Hogan, R. J.: Combined CloudSat-CALIPSO-MODIS retrievals of the properties of ice clouds, J. Geophys. Res., 115, D00H29, https://doi.org/10.1029/2009JD012346, 2010.

Delanoë, J., Hogan, R. J., Forbes, R. M., Bodas-Salcedo, A., and Stein, T. H. M.: Evaluation of ice cloud representation in the ECMWF and UK Met Office models using CloudSat and CALIPSO data, Quart. J. Roy. Meteor. Soc., 137, 2064–2078, 2011.

ECMWF: IFS Documentation – Cy41r2. Part IV: Physical Processes, European Centre for Medium-Range Weather Forecasts, Reading, U.K., 2016.

Eliasson, S., Holl, G., Buehler, S. A., Kuhn, T., Stengel, M., Iturbide-Sanchez, F., and Johnston, M.: Systematic and random errors between collocated satellite ice water path observations, J. Geophys. Res., 118, 2629–2642, 2013.

Field, P. R., Bodas-Salcedo, A., and Brooks, M. E.: Using model analysis and satellite data to assess cloud and precipitation in midlatitude cyclones, Quart. J. Roy. Meteor. Soc., 137, 1501–1515, 2011.

Flaounas, E., Lagouvardos, K., Kotroni, V., Claud, C., Delanoë, J., Flamant, C., Madonna, E., and Wernli, H.: Processes leading to heavy precipitation associated with two Mediterranean cyclones observed during the HyMeX SOP1, Quart. J. Roy. Meteor. Soc., 142, 275–286, 2016.

Flaounas, E., Kotroni, V., Lagouvardos, K., Gray, S. L., Rysman, J.-F., and Claud, C.: Heavy rainfall in Mediterranean cyclones. Part I: contribution of deep convection and warm conveyor belt, Clim. Dyn., 50, 2935–2949, 2018.

Forbes, R. M. and Ahlgrimm, M.: On the representation of high-latitude boundary layer mixed-phase cloud in the ECMWF global model, Mon. Wea. Rev., 142, 3425–3445, 2014.

Gehring, J., Oertel, A., Vignon, E., Jullien, N., Besic, N., and Berne, A.: Microphysics and dynamics of snowfall associated with a warm conveyor belt over Korea, Atmos. Chem. Phys, 20, 7373–7392, 2020.

Grams, C. M., Wernli, H., Böttcher, M., Čampa, J., Corsmeier, U., Jones, S. C., Keller, J. H., Lenz, C.-J., and Wiegand, L.: The key role of diabatic processes in modifying the upper-tropospheric wave guide: a North Atlantic case-study, Quart. J. Roy. Meteor. Soc., 137, 2174–2193, 2011.

Grams, C. M., Magnusson, L., and Madonna, E.: An atmospheric dynamics perspective on the amplification and propagation of forecast error in numerical weather prediction models: A case study, Quart. J. Roy. Meteor. Soc., 144, 2577–2591, 2018.

Gray, S. L., Dunning, C. M., Methven, J., Masato, G., and Chagnon, J. M.: Systematic model forecast error in Rossby wave structure, Geophys. Res. Lett., 41, 2979–2987, 2014.

Harrold, T. W.: Mechanisms influencing the distribution of precipitation within baroclinic disturbances, Quart. J. Roy. Meteor. Soc., 99, 232–251, 1973.

Haynes, J. M., L'Ecuyer, T. S., Stephens, G. L., Miller, S. D., Mitrescu, C., Wood, N. B., and Tanelli, S.: Rainfall retrieval over the ocean with spaceborne W-band radar, J. Geophys. Res., 114, D00A22, https://doi.org/10.1029/2008JD009973, 2009.

Hersbach, H., Bell, W., Berrisford, P., Horányi, A., Muñoz-Sabater, J., Nicolas, J., Radu, R., Schepers, D., Simmons, A., Soci, C., and Dee, D.: Global reanalysis: goodbye ERA-Interim, hello ERA5, ECMWF Newsletter, 159, 17–24, 2019.

Hersbach, H., Bell, B., Berrisford, P., Hirahara, S., Horányi, A., Muñoz-Sabater, J., Nicolas, J., Peubey, C., Radu, R., Schepers, D., et al.: The ERA5 global reanalysis, Quart. J. Roy. Meteor. Soc., 146, 1999–2049, 2020.

Heymsfield, A. J., Bansemer, A., Matrosov, S., and Tian, L.: The 94-GHz radar dim band: Relevance to ice cloud properties and CloudSat, Geophys. Res. Lett., 35, 2008.

Illingworth, A. J., Hogan, R. J., O'Connor, E. J., Bouniol, D., Brooks, M. E., Delanoë, J., Donovan, D. P., Eastment, J. D., Gaussiat, N., Goddard, W. F., Haeffelin, M., Klein Baltink, H., Krasnov, O. A., Pelon, J., Pirou, J.-M., Protat, A., Russchenberg, H. W. J., Seifert, A., Tompkins, A. M., Zadelhoff, G.-J., Vinit, F., Willén, U., Wilson, D. R., and Wrench, C. L.: Cloudnet – Continuous evaluation of cloud profiles in seven operational models using ground-based observations, Bull. Amer. Meteor. Soc., 88, 883, 2007.

Joos, H. and Forbes, R. M.: Impact of different IFS microphysics on a warm conveyor belt and the downstream flow evolution, Quart. J. Roy. Meteor. Soc., 142, 2727–2739, 2016.

Joos, H. and Wernli, H.: Influence of microphysical processes on the potential vorticity development in a warm conveyor belt: a case-study with the limited-area model COSMO, Quart. J. Roy. Meteor. Soc., 138, 407–418, 2012.

650 Klein, S. A., McCoy, R. B., Morrison, H., Ackerman, A. S., Avramov, A., Boer, G. d., Chen, M., Cole, J. N. S., Del Genio, A. D., Falk, M., et al.: Intercomparison of model simulations of mixed-phase clouds observed during the ARM Mixed-Phase Arctic Cloud Experiment. I: Single-layer cloud, Quart. J. Roy. Meteor. Soc., 135, 979–1002, 2009.

Knapp, K. R., Ansari, S., Bain, C. L., Bourassa, M. A., Dickinson, M. J., Funk, C., Helms, C. N., Hennon, C. C., Holmes, C. D., Huffman, G. J., et al.: Globally gridded satellite observations for climate studies, Bull. Amer. Meteor. Soc., 92, 893–907, 2011.

655 Kunkel, D., Hoor, P., and Wirth, V.: The tropopause inversion layer in baroclinic life-cycle experiments: the role of diabatic processes, Atmos. Chem. Phys, 16, 2016.

Mace, G. G., Marchand, R., Zhang, Q., and Stephens, G.: Global hydrometeor occurrence as observed by CloudSat: Initial observations from summer 2006, Geophys. Res. Lett., 34, L09 808, https://doi.org/10.1029/2006GL029017, 2007.

Madonna, E., Wernli, H., Joos, H., and Martius, O.: Warm conveyor belts in the ERA-Interim dataset (1979–2010). Part I: Climatology and 660 potential vorticity evolution, J. Climate, 27, 3–26, 2014.

Madonna, E., Boettcher, M., Grams, C. M., Joos, H., Martius, O., and Wernli, H.: Verification of North Atlantic warm conveyor belt outflows in ECMWF forecasts, Quart. J. Roy. Meteor. Soc., 141, 1333–1344, 2015.

Marchand, R., Mace, G. G., Ackerman, T., and Stephens, G.: Hydrometeor detection using CloudSat-An Earth-orbiting 94-GHz cloud radar, J. Atmos. Oceanic Technol., 25, 519–533, 2008.

665 Martínez-Alvarado, O. and Plant, R. S.: Parametrized diabatic processes in numerical simulations of an extratropical cyclone, Quart. J. Roy. Meteor. Soc., 140, 1742–1755, 2014.

Morrison, H., Shupe, M. D., and Curry, J. A.: Modeling clouds observed at SHEBA using a bulk microphysics parameterization implemented into a single-column model, J. Geophys. Res., 108, 4255, https://doi.org/10.1029/2002JD002229, 2003.

Naud, C. M., Del Genio, A. D., Bauer, M., and Kovari, W.: Cloud vertical distribution across warm and cold fronts in CloudSat-CALIPSO 670 data and a general circulation model, J. Climate, 23, 3397–3415, 2010.

Naud, C. M., Posselt, D. J., and Van Den Heever, S. C.: Observational analysis of cloud and precipitation in midlatitude cyclones: Northern versus Southern Hemisphere warm fronts, J. Climate, 25, 5135–5151, 2012.

Naud, C. M., Booth, J. F., and Del Genio, A. D.: Evaluation of ERA-Interim and MERRA cloudiness in the Southern Ocean, J. Climate, 27, 2109–2124, 2014.

675 Naud, C. M., Posselt, D. J., and van den Heever, S. C.: A CloudSat–CALIPSO view of cloud and precipitation properties across cold fronts over the global oceans, Journal of Climate, 28, 6743–6762, 2015.

Neiman, P. J., Shapiro, M. A., and Fedor, L. S.: The life cycle of an extratropical marine cyclone. Part II: Mesoscale structure and diagnostics, Mon. Wea. Rev., 121, 2177–2199, 1993.

Oertel, A., Boettcher, M., Joos, H., Sprenger, M., Konow, H., Hagen, M., and Wernli, H.: Convective activity in an extratropical cyclone and 680 its warm conveyor belt–a case-study combining observations and a convection-permitting model simulation, Quart. J. Roy. Meteor. Soc., 145, 1406–1426, 2019.

Oertel, A., Boettcher, M., Joos, H., Sprenger, M., and Wernli, H.: Potential vorticity structure of embedded convection in a warm conveyor belt and its relevance for large-scale dynamics, Weather Clim. Dynam., 1, 127–153, 2020.

Posselt, D. J., Stephens, G. L., and Miller, M.: CLOUDSAT adding a new dimension to a classical view of extratropical cyclones, Bull. Amer. 685 Meteor. Soc., 89, 599, 2008.

Rossa, A. M., Wernli, H., and Davies, H. C.: Growth and decay of an extra-tropical cyclone's PV-tower, Meteor. Atmos. Phys., 73, 139–156, 2000.

Sassen, K., Matrosov, S., and Campbell, J.: CloudSat spaceborne 94 GHz radar bright bands in the melting layer: An attenuation-driven upside-down lidar analog, Geophys. Res. Lett., 34, 2007.

690 Schäfler, A. and Harnisch, F.: Impact of the inflow moisture on the evolution of a warm conveyor belt, Quart. J. Roy. Meteor. Soc., 141, 299–310, 2015.

Schäfler, A., Dörnbrack, A., Wernli, H., Kiemle, C., and Pfahl, S.: Airborne lidar observations in the inflow region of a warm conveyor belt, Quart. J. Roy. Meteor. Soc., 137, 1257–1272, 2011.

Sprenger, M. and Wernli, H.: The LAGRANTO Lagrangian analysis tool – version 2.0, Geosci. Model Dev., 8, 2569–2586, 2015.

695 Sprenger, M., Fragkoulidis, G., Binder, H., Croci-Maspoli, M., Graf, P., Grams, C. M., Knippertz, P., Madonna, E., Schemm, S., Škerlak, B., et al.: Global climatologies of Eulerian and Lagrangian flow features based on ERA-Interim, Bull. Amer. Meteor. Soc., 98, 1739–1748, 2017.

Stein, T. H. M., Delanoë, J., and Hogan, R. J.: A comparison among four different retrieval methods for ice-cloud properties using data from CloudSat, CALIPSO, and MODIS, J. Appl. Meteor. Climatol., 50, 1952–1969, 2011.

700 Stephens, G. L. and Haynes, J. M.: Near global observations of the warm rain coalescence process, Geophys. Res. Lett., 34, L20 805, https://doi.org/10.1029/2007GL030259, 2007.

Stephens, G. L., Vane, D. G., Boain, R. J., Mace, G. G., Sassen, K., Wang, Z., Illingworth, A. J., O'Connor, E. J., Rossow, W. B., Durden, S. L., et al.: The CloudSat mission and the A-Train: A new dimension of space-based observations of clouds and precipitation, Bull. Amer. Meteor. Soc., 83, 1771–1790, 2002.

705 Stephens, G. L., Vane, D. G., Tanelli, S., Im, E., Durden, S., Rokey, M., Reinke, D., Partain, P., Mace, G. G., Austin, R., et al.: CloudSat mission: Performance and early science after the first year of operation, J. Geophys. Res., 113, D00A18, https://doi.org/10.1029/2008JD009982, 2008.

Tanelli, S., Durden, S. L., Im, E., Pak, K. S., Reinke, D. G., Partain, P., Haynes, J. M., and Marchand, R. T.: CloudSat's cloud profiling radar after two years in orbit: Performance, calibration, and processing, IEEE Trans. Geosci. Remote Sens., 46, 3560–3573, 2008.

710 Tiedtke, M.: A comprehensive mass flux scheme for cumulus parameterization in large-scale models, Mon. Wea. Rev., 117, 1779–1800, 1989.

Tiedtke, M.: Representation of clouds in large-scale models, Mon. Wea. Rev., 121, 3040–3061, 1993.

Wernli, H. and Davies, H. C.: A Lagrangian-based analysis of extratropical cyclones. I: The method and some applications, Quart. J. Roy. Meteor. Soc., 123, 467–489, 1997.

715 Wernli, H. and Schwierz, C.: Surface cyclones in the ERA-40 dataset (1958-2001). Part I: Novel identification method and global climatology, J. Atmos. Sci., 63, 2486–2507, 2006.

Wernli, H., Boettcher, M., Joos, H., Miltenberger, A. K., and Spichtinger, P.: A trajectory-based classification of ERA-Interim ice clouds in the region of the North Atlantic storm track, Geophys. Res. Lett., 43, 6657–6664, 2016.

Winker, D. M., Pelon, J. R., and McCormick, M. P.: The CALIPSO mission: spaceborne lidar for observation of aerosols and clouds, Proc.
720 SPIE, 4893, 1–11, 2003.

Winker, D. M., Vaughan, M. A., Omar, A., Hu, Y., Powell, K. A., Liu, Z., Hunt, W. H., and Young, S. A.: Overview of the CALIPSO mission and CALIOP data processing algorithms, J. Atmos. Oceanic Technol., 26, 2310–2323, 2009.
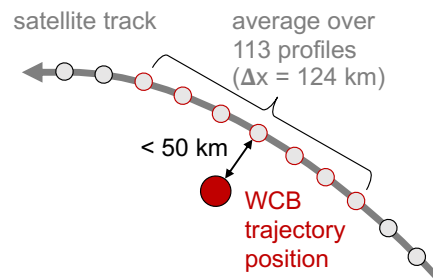
Figure 1. Schematic illustration of the method to attribute several satellite profiles to a matching ERA5-based WCB trajectory in the climatological analysis.
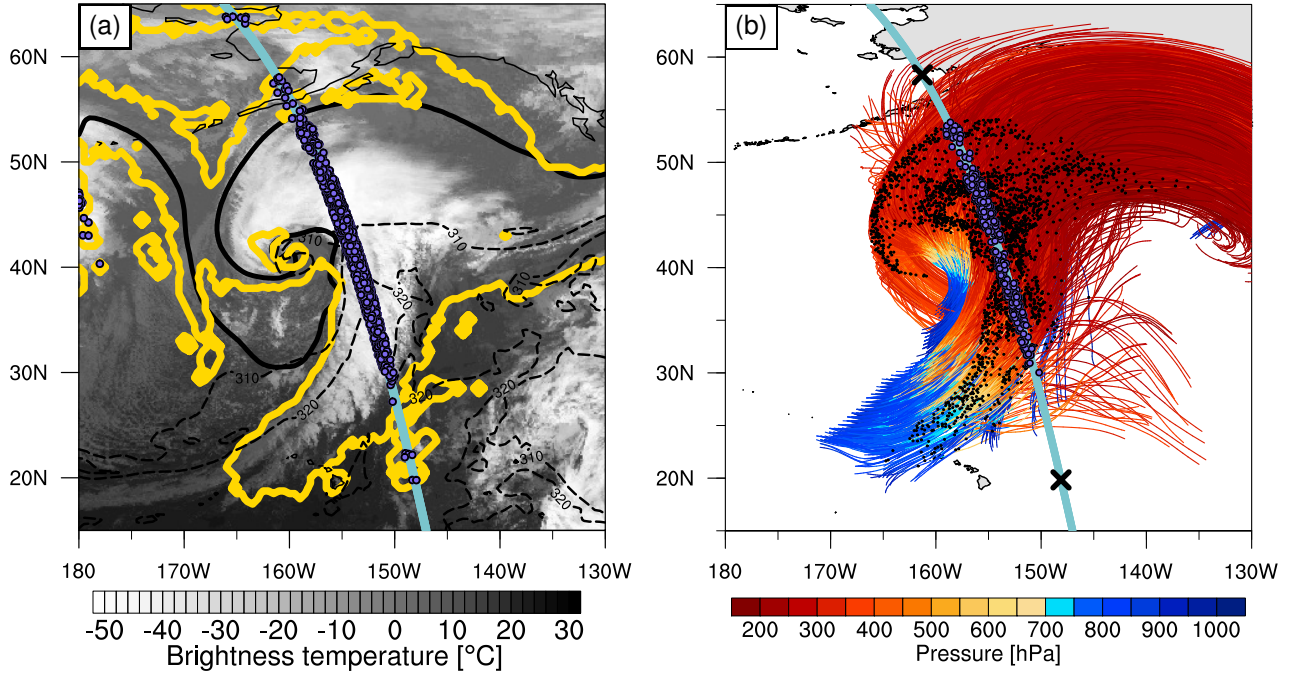
Figure 2. Case study of a North Pacific WCB at 00 UTC 3 January 2014. (a) Infrared satellite image (brightness temperature in °C) derived from the GridSat-B1 data (Knapp et al., 2011), and, from ERA5, the 2-pvu contour on 315 K (black solid), θ_e (black dashed contours at 310 and 320 K) and grid points with at least one WCB trajectory (yellow). The blue line marks the track of the A-Train, and the purple dots show matches between WCB air parcels and the satellite track. (b) Two-day WCB trajectories (coloured by pressure; hPa) starting at 06 UTC 2 Jan 2014. The positions of the trajectories at the time of the satellite overpass, at 00 UTC 3 Jan, are shown by black and purple dots, with the purple dots indicating matches with the satellite track (blue line). The ~~blue line again marks the track~~ segment of the ~~A-Train, and the segment~~ satellite track between the two black crosses indicates the region shown in Fig. 3.
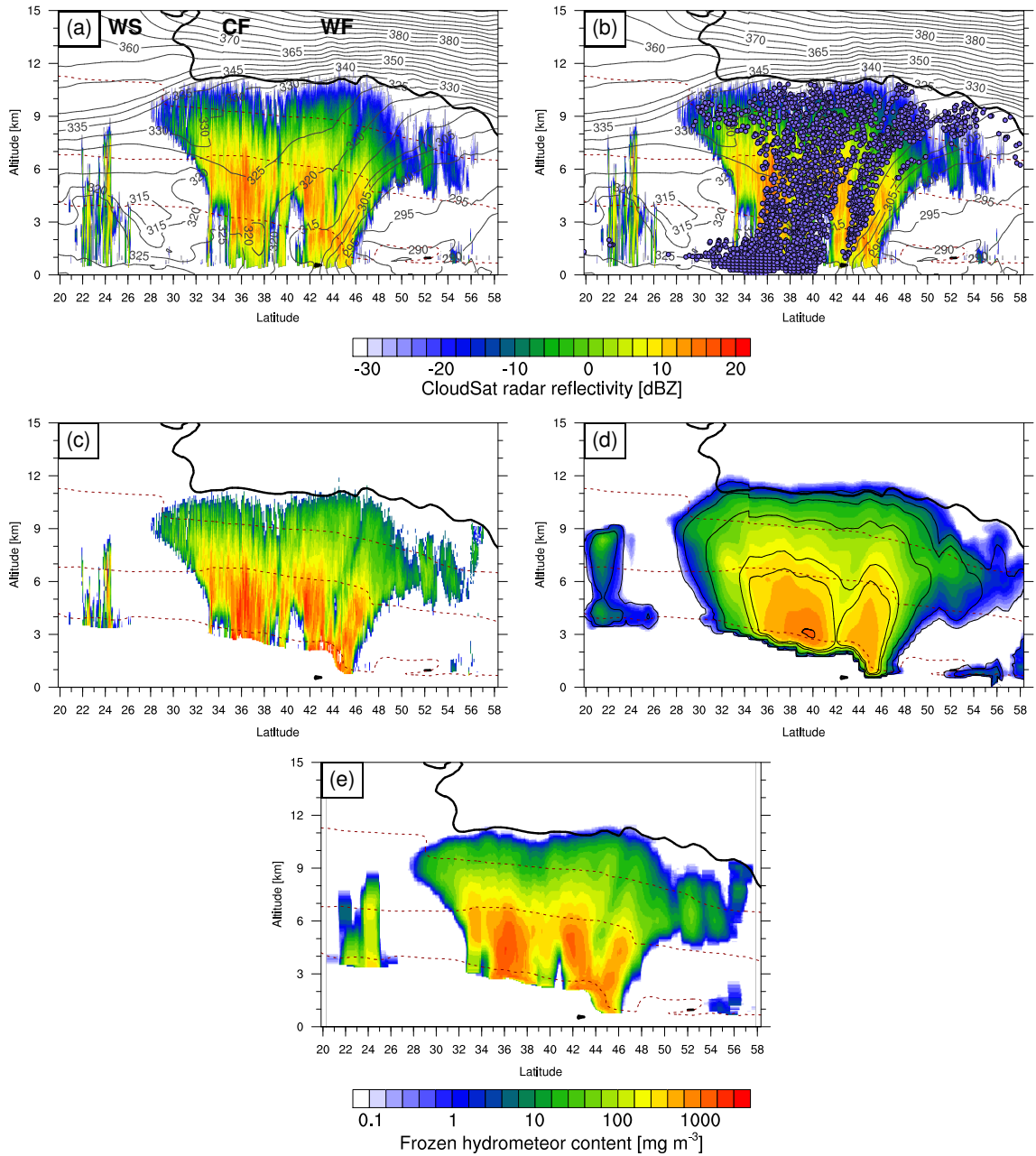
Figure 3. Vertical cross sections of observed and modelled variables along a North Pacific WCB at 00 UTC 3 January 2014. (a) CloudSat radar reflectivity (dBZ; shading) along the segment between the two black crosses in Fig. 2b, together with, from ERA5, interpolated θ_e (black contours every 5 K), temperature (red dashed contours at $0°$, $-20°$ and $-40°$C) and the 2-pvu contour (thick black line). The labels mark the position of the warm sector ("WS"), the cold front ("CF") and the warm front ("WF"), respectively. (b) Same as (a), but with the positions of the intersected WCB trajectories shown by the purple dots. (c) DARDAR-retrieved IWC (mg m^{-3}; shading), which consists of the entire frozen hydrometeor content, i.e., ice and falling snow, (d) ERA5-based frozen hydrometeor content, i.e., the sum of ~~IWC~~ the prognostic cloud ice and ~~SWC~~ snow water contents (mg m^{-3}; shading), and ~~SWC~~ prognostic snow water content only (thin black contours at 0.1, 1, 10, 100, 200 and 1000 mg m^{-3}), and (e) DARDAR-retrieved IWC in a running mean along 113 satellite profiles (corresponding to a segment of ~ 124 km). The thick black line in (c-e) again marks the 2-pvu contour, and the red dashed lines the $0°$, $-20°$ and $-40°$C isotherms.
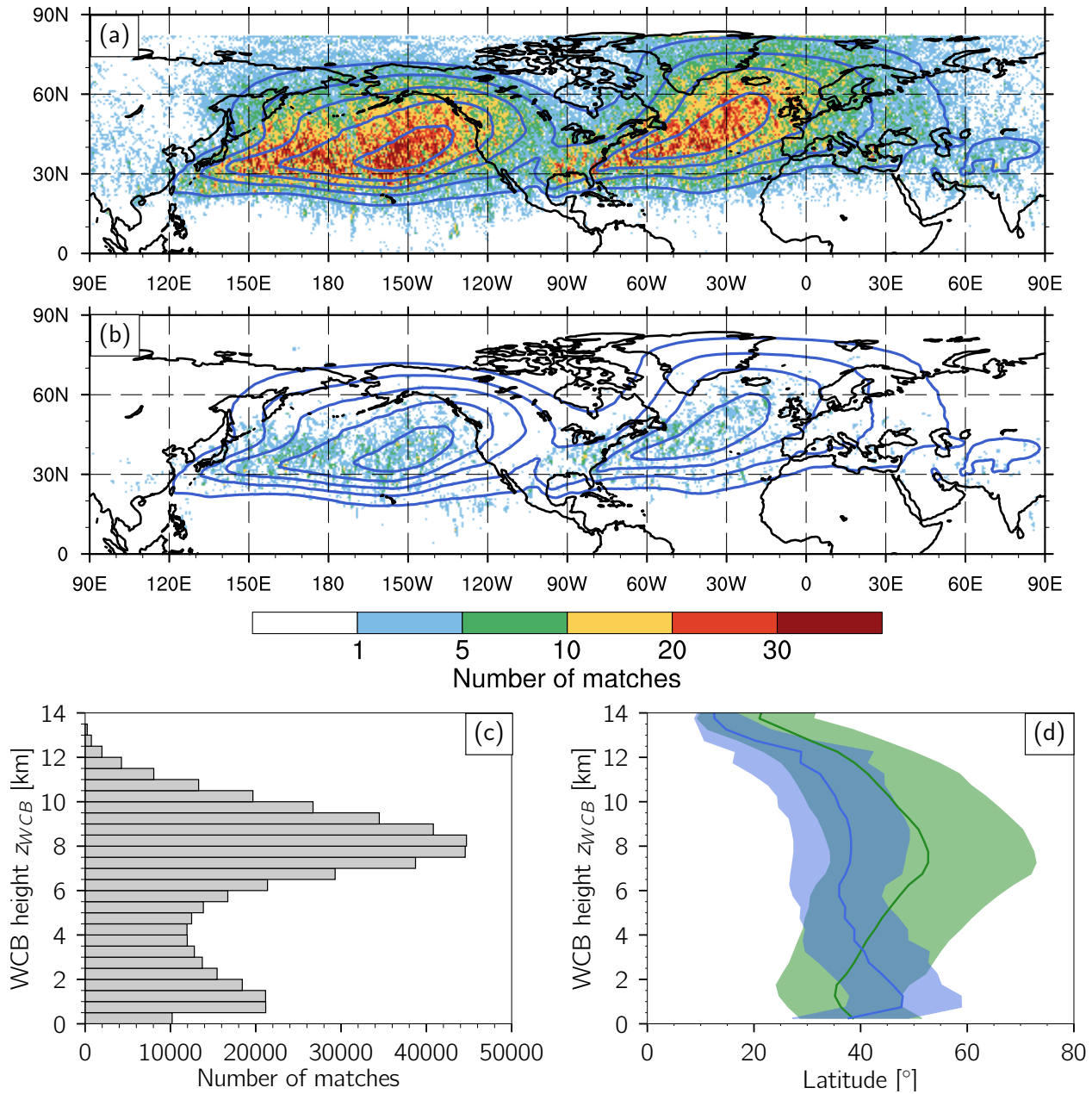
Figure 4. (a) Spatial distribution of the WCB trajectories matching with the satellite track (shading). The colours indicate the number of matches ~~in~~ at each ~~0.5° bin~~grid point. Overlaid is the ERA5-based climatological frequency of WCB trajectories for December-February 1980-2018 (blue contours every 10%), whereby all time steps between the start (~~t=0~~$t = 0$ h) and the end (~~t=48~~$t = 48$ h) of the trajectories are considered. (b) As in (a), but for strong WCBs, i.e., the top 5% of the matches with highest reflectivity values in each vertical height bin. (c) Height distribution of the matches, and (d) latitude of the matches as a function of their height for all WCBs (~~black and grey~~green) and strong WCBs (~~red~~blue). The ~~thick black~~ green and ~~red~~ blue lines show the mean over the matches, and the ~~grey and red shading~~ shadings represent the range between the ~~10%~~10th and the ~~90%~~90th percentile.

26
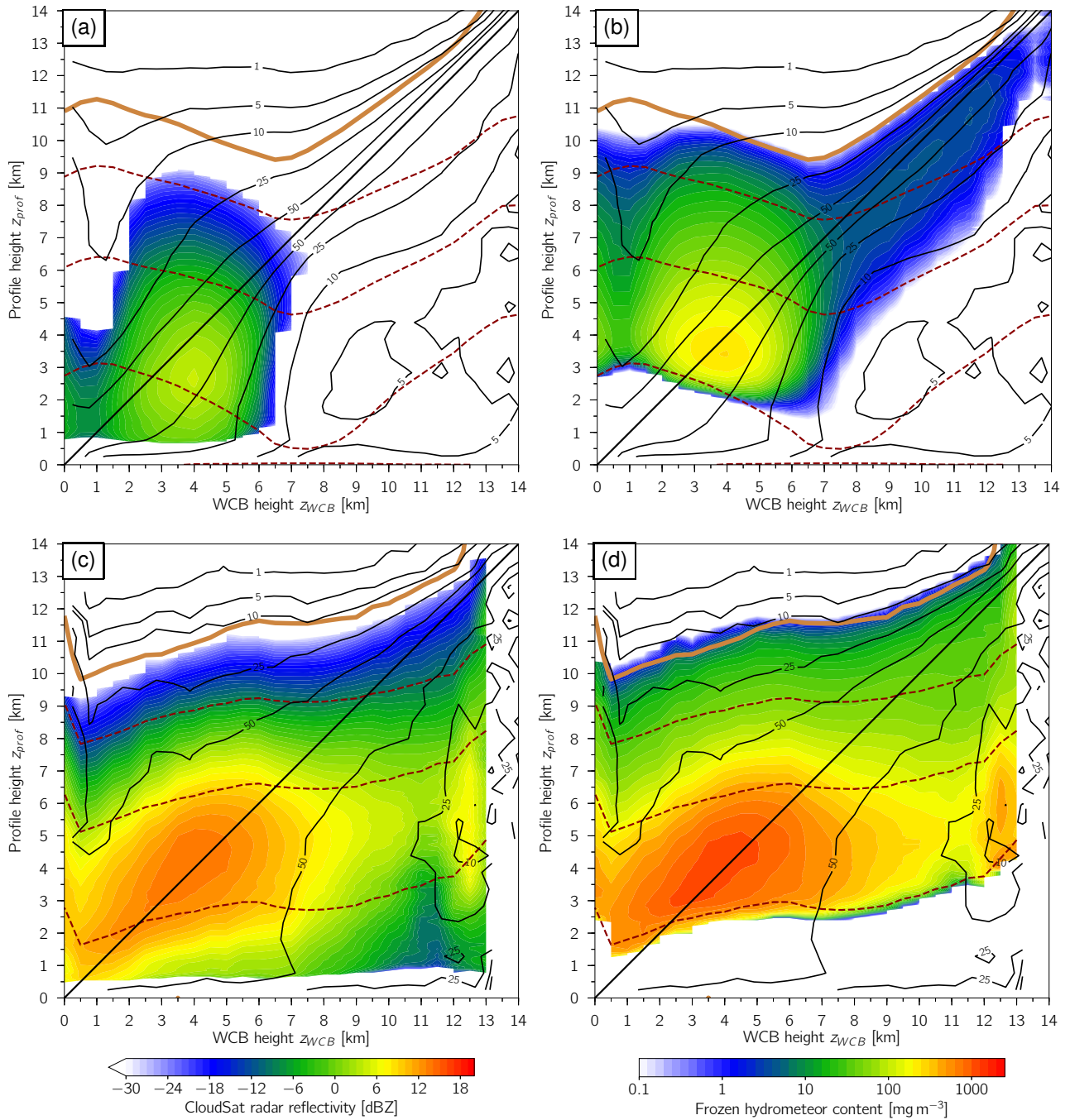
Figure 5. Composites for all WCBs (top panels) and strong WCBs (bottom panels) of the median vertical profiles of (a, c) CloudSat radar reflectivity (dBZ; shading) and (b, d) DARDAR-retrieved IWC (mg m^{-3}; shading), separately for different height bins of the matching WCB air parcels (see text for details). The DARDAR-retrieved IWC in (b, d) consists of the entire frozen hydrometeor content, i.e., ice and falling snow. The black lines show the relative WCB trajectory frequency at each profile height (contours at 1, 5, 10, 25, 50 and 100%), the red dashed line the temperature (contours at 0°, −20° and −40°C), and the brown line the 2-pvu contour, all three fields interpolated from ERA5.
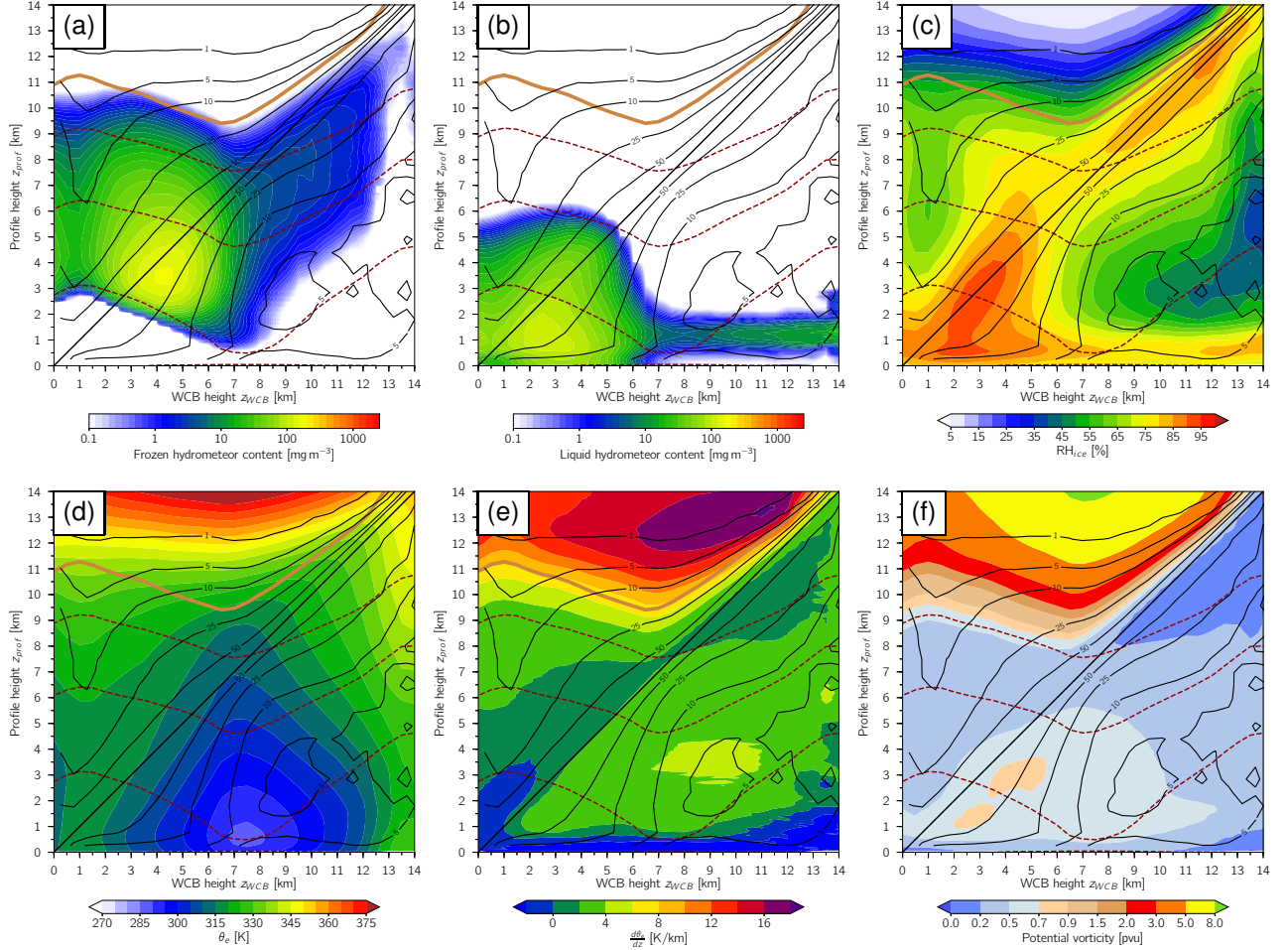
Figure 6. Composite over all WCBs of the (a, b) median and (c-f) mean vertical profiles of ERA5 fields, separately for different height bins of the matching WCB air parcels. The shading shows (a) the ~~sum of IWC and SWC~~ frozen hydrometeor content (mg m^{-3}), ~~(b)~~ i.e., the sum of ~~LWC~~ the prognostic cloud ice and ~~RWC~~ snow water contents, (b) the liquid hydrometeor content (mg m^{-3}), i.e., the sum of the prognostic cloud liquid water and rain water contents, (c) relative humidity with respect to ice (%), (d) θ_e (K), (e) moist vertical stability $d\theta_e/dz$ (K km^{-1}), and (f) PV (pvu). The black and brown contours are as in Fig. 5.
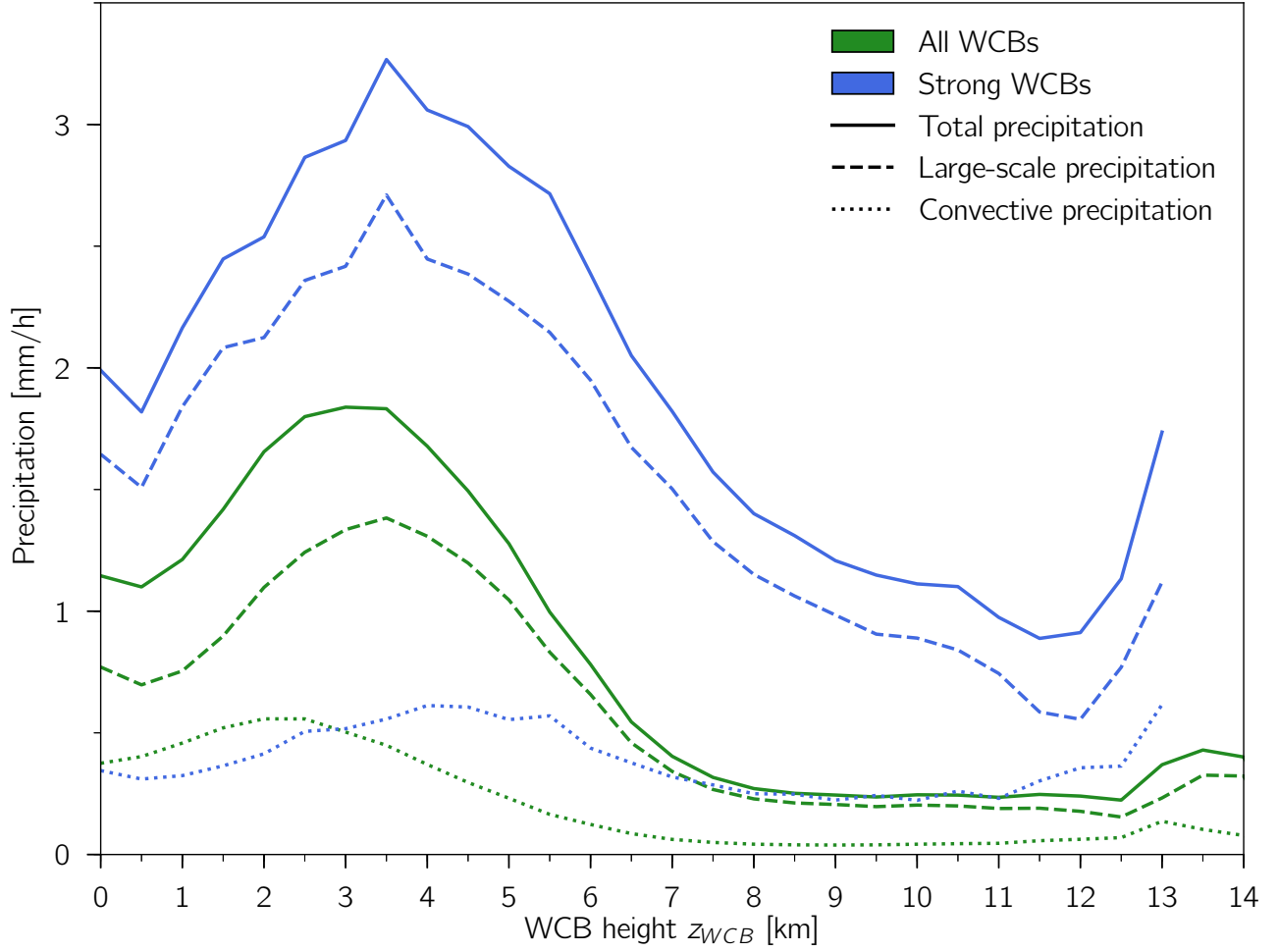
Figure 7. ERA5-based total (solid), large-scale (long-dashed) and convective (short-dashed) surface precipitation accumulated during the previous hour, averaged over all (green) and strong WCBs (blue), separately for different height bins of the matching WCB air parcels.
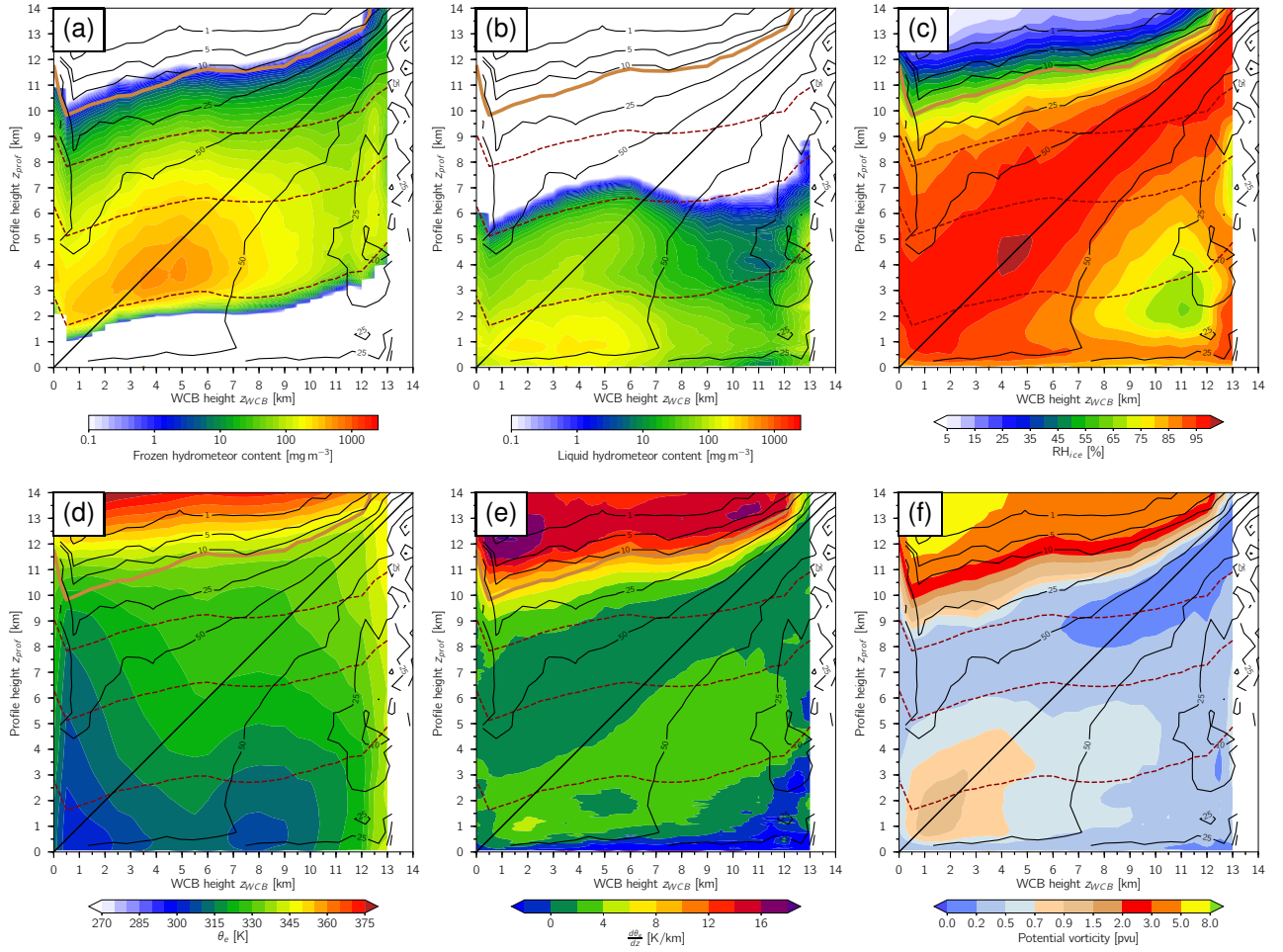
Figure 8. As Fig. 6, but for the category of strong WCBs.